

AD-A067 017

AIR FORCE GEOPHYSICS LAB HANSCOM AFB MASS  
ASPECT DETERMINATION FOR THE AFGL INFRARED SURVEY EXPERIMENTS.(U)  
OCT 78 S D PRICE, D S AKERSTROM, C V CUNIFF  
AFGL-TR-78-0253

F/6 3/1

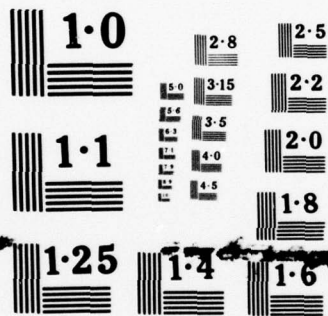
UNCLASSIFIED

NL

1 OF 1  
ADA  
067017



END  
DATE  
FILMED  
6-79  
DDC



NATIONAL BUREAU OF STANDARDS  
MICROCOPY RESOLUTION TEST CHART

**LEVEL** *12*

AFGL-TR-78-0253  
INSTRUMENTATION PAPERS, NO. 272



## Aspect Determination for the AFGL Infrared Survey Experiments

STEPHAN D. PRICE  
DAVID S. AKERSTROM  
CHARLES V. CUNIFF  
LEONARD P. MARCOTTE  
PETER C. TANDY  
RUSSELL G. WALKER



16 October 1978

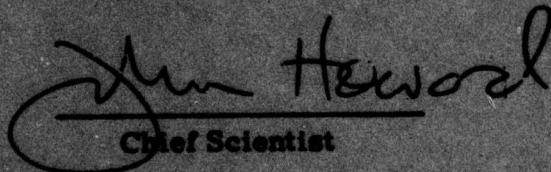
Approved for public release; distribution unlimited.

OPTICAL PHYSICS DIVISION    PROJECT 7670

This report has been reviewed by the ESD Information Office (O) releasable to the National Technical Information Service (NTIS).

This technical report has been reviewed and is approved for publication.

FOR THE COMMANDER

  
Chief Scientist

Qualified requestors may obtain additional copies from the Defense Documentation Center. All others should apply to the National Technical Information Service.



Unclassified

SECURITY CLASSIFICATION OF THIS PAGE (When Data Entered)

REPORT DOCUMENTATION PAGE		READ INSTRUCTIONS BEFORE COMPLETING FORM
1. REPORT NUMBER	2. GOVT ACCESSION NO.	3. RECIPIENT'S CATALOG NUMBER
AFGL-TR-78-0253	AFGL-IP-272	
4. TITLE (and Subtitle)	5. TYPE OF REPORT & PERIOD COVERED	
ASPECT DETERMINATION FOR THE AFGL INFRARED SURVEY EXPERIMENTS,	Scientific. Interim.	
7. AUTHOR(s)	6. PERFORMING ORG. REPORT NUMBER	
Stephan D./Price, Leonard P./Marcotte David S./Akerstrom, Peter C./Tandy Charles V./Cunniff, Russell G. Walker*	IP No. 272	
9. PERFORMING ORGANIZATION NAME AND ADDRESS	8. CONTRACT OR GRANT NUMBER(s)	
Air Force Geophysics Laboratory (OP) Hanscom AFB Massachusetts 01731		
11. CONTROLLING OFFICE NAME AND ADDRESS	10. PROGRAM ELEMENT, PROJECT, TASK AREA & WORK UNIT NUMBERS	
Air Force Geophysics Laboratory (OP) Hanscom AFB Massachusetts 01731	16 62101F 17 06 76700608	
14. MONITORING AGENCY NAME & ADDRESS (if different from Controlling Office)	12. REPORT DATE	
Instrumentation papers,	11 16 October 1978	
	13. NUMBER OF PAGES	
	48	
	15. SECURITY CLASS. (of this report)	
	Unclassified	
	15a. DECLASSIFICATION/DOWNGRADING SCHEDULE	
16. DISTRIBUTION STATEMENT (of this Report)		
Approved for public release; distribution unlimited. 12 48p.		
17. DISTRIBUTION STATEMENT (of the abstract entered in Block 20, if different from Report)		
18. SUPPLEMENTARY NOTES		
* Present Address: NASA Ames Research Center Moffett, CA 94035		
19. KEY WORDS (Continue on reverse side if necessary and identify by block number)		
Infrared Astronomy Aspect determination Pointing accuracy		
20. ABSTRACT (Continue on reverse side if necessary and identify by block number)		
<p>The AFGL probe borne infrared celestial survey experiments are designed to obtain the inertial aspect of the payload reference frame with an accuracy comparable to the spatial size of a resolution element in the infrared telescope. Constraining the axis of payload rotation to known inertial coordinates through maintaining lock onto a selected pole star with a star tracker co-aligned to the roll-axis, and by careful geometric alignment of the optical elements and dynamic balancing the payload, the desired accuracy was achieved. Further</p>		

DD FORM 1 JAN 73 1473 EDITION OF 1 NOV 65 IS OBSOLETE

Unclassified

SECURITY CLASSIFICATION OF THIS PAGE (When Data Entered)

409 578

79 04 05 002 LB

next page

Unclassified

SECURITY CLASSIFICATION OF THIS PAGE(When Data Entered)

20. Abstract (Continued)

refinement in position was obtained from the stellar detections by the infrared sensor, with an ultimate knowledge of the inertial aspect being within 1.5 arc minutes root mean square deviation between the measured and catalogued positions for known infrared stars. The procedures used to obtain this accuracy are described. Also detailed is a method of aspect determination using only a star mapper with an N slit focal plane reticle.

Unclassified

SECURITY CLASSIFICATION OF THIS PAGE(When Data Entered)

## Preface

We gratefully acknowledge the fine efforts of those who were instrumental in designing and implementing the experiment.

The overall design of the payload instrumentation system and telescope mounting was developed by the Aerospace Instrument Laboratory of AFGL under the direction of C. Nealon Stark, whose ingenuity and depth of engineering experience were essential to the success of the rocket program. Paul Hartnett, Daniel Nardello, Edward LeBlanc, Laurence Smart and Thomas Campbell of Wentworth Institute were responsible for the payload construction and assembly and assisted in the alignment measurements.

Dr. Thomas L. Murdock deserves special mention for his many helpful discussions and his tireless assistance during the field alignments.

ACCESSION for	
NTIS	White Section <input checked="" type="checkbox"/>
DOC	Buff Section <input type="checkbox"/>
UNANNOUNCED	
JUSTIFICATION	
BY	
DISTRIBUTION/AVAILABILITY NOTES	
Dis	DATE
A	



## Contents

1. INTRODUCTION	7
2. GEOMETRIC REFERENCE	9
3. DYNAMIC ALIGNMENT	13
4. EXPERIMENTAL PROFILE	16
5. AZIMUTH ASPECT	19
6. ASPECT UPDATES THROUGH THE INFRARED SENSOR	25
7. COMPLETE ATTITUDE DETERMINED WITH THE STAR MAPPER	30
8. RESULTS AND CONCLUSIONS	43
REFERENCES	45
APPENDIX: Definition of Terms	47

## Illustrations

1. Payload Showing the Infrared Telescope in the Stowed Position	10
2. The Payload Diagram	10
3. A Map of the "N" Slit Reticle for a Star Mapper Used on One of the Survey Flights	12

## Illustrations

4. Payload Mounted on the Dynamic Balancer	14
5. The Constraining Fixture for the Balancer	15
6. Experimental Geometry	18
7. Comparison Between the Calculated Output of the Star Mapper and the Observed Output	20
8. The Distribution in the Calculated Uncertainties of the Right Ascensions, Reduced to the Equator, of all the Sources in the AFGL Catalog <sup>2</sup>	28
9. The Distributions in the Calculated Uncertainties in Declination for the Sources in the AFGL Catalog	28
10. The Distribution of the Differences Between Right Ascensions Reduced to the Equator, of IRC <sup>6, 7</sup> Sources in the AFGL Catalog and the Listed Position Either in the IRC <sup>6, 7</sup> or the SAO <sup>8</sup> Catalog	29
11. A Histogram of the Differences in the Declination of AFGL Sources and the IRC <sup>6, 7</sup> Objects Associated With Them	29
12. The Geometry of the Experiment	31
13. Geometry of a Star Transit	34
14. Pole of Rotation in Inertial Coordinates	37

## Aspect Determination for the AFGL Infrared Survey Experiments

### 1. INTRODUCTION

A celestial survey involves a compromise between the objectives to cover large areas of the sky at high sensitivity with good spectral and spatial resolution and the constraints of finite observing time and physical limitations on the instruments. The AFGL Infrared Sky Survey (Walker and Price;<sup>1</sup> Price and Walker;<sup>2</sup> Price<sup>3</sup>) obtained broad band observations in the 3 to 30 microns spectral regions at moderate sensitivities and with sufficient spatial resolution to enable ground based telescopes to acquire, with moderate effort, the unidentified sources found on the survey.

The AFGL Survey was conducted by flying cryogenically cooled telescopes on sounding rockets. The advantage of flying the sensors above the atmosphere is that the background irradiance from the atmosphere and telescope is eliminated, which permits high sensitivity photoconductors to be used with large fields-of-view.

---

(Received for publication 13 October 1978)

1. Walker, R. G., and Price, S. D. (1975) AFGL Infrared Sky Survey: Volume I. Catalog of Observations at 4, 11 and 20 Microns, AFGL-TR-75-0373.
2. Price, S. D., and Walker, R. G. (1976) The AFGL Four Color Infrared Sky Survey: Catalog of Observations at 4.2, 11.0, 19.8 and 27.4  $\mu$ m, AFGL-TR-76-0208.
3. Price, S. D. (1977) The AFGL Four Color Infrared Sky Survey: Supplemental Catalog, AFGL-TR-77-0160.



On the other hand, the observing time and the size of the instrumentation that can be flown are limited by the performance of the rocket.

The ultimate limit to the positional accuracy of the sources detected during the survey was defined by the size of the detector elements. The sensor focal plane was composed of three linear staggered arrays of detectors, one in each spectral band. Each detector element had an instantaneous field-of-view of 0.975 by 3.05 milliradians (3.35 by 10.5 arc min) and overlapped the adjacent detector by 0.5 milliradians (1.7 arc min), approximately of the order of the diffraction blur circle diameter at 10 microns. The positional uncertainty associated with a resolution element was, therefore, 1 to 2 arc min.

The instrumentation, payload structure and experimental profile were designed to allow determination of aspect independently of the celestial radiometer with an accuracy at least as good as defined by the detector resolution. Drift rates for inertial platforms available in the early 1970's were too large to maintain the arc min attitude reference of the rotation axis under the dynamic requirements of the experiment. An ITT "Fine Guidance Error Sensor," (star tracker), was incorporated into an Aerojet Liquid Rocket Company (ALRC) MARK II attitude control system (ACS) to provide the required accuracy and stability.

The star tracker was aligned to the longitudinal axis of the payload which was made to be co-lateral with the roll axis of the ACS. During the survey portion of the flight, the star tracker locked onto a star selected to be near local zenith and maintained the roll axis to within the required 20 arc sec while the payload was rotated to generate the survey scan. The infrared sensor was deployed on a one axis gimbal to pre-programmed zenith angles. The deployment positions were measured to one arc min digitization resolution by means of an optical encoder mounted on the gimbal shaft. The zenith angles were changed each time the ACS sensed the completion of a 360 degree roll.

The azimuthal aspect for each roll was determined from data obtained from stellar transits detected by a stellar aspect sensor (star mapper). This instrument consists of a small telescope, an "N" slit focal plane mask and a Fabrey field lens to image the primary objective onto an S-11 photomultiplier.

An accurate geometric reference was established between the star tracker and star mapper with the infrared telescope position determined as a function of optical shaft encoder readout prior to the flights. During all the flights, the star tracker maintained the rotation axis to within 20 arc sec, the star mapper observations were used to obtain a polynomial fit of azimuth as a function of time to one to 1.5 arc min root mean square accuracy for each roll, and the optical shaft encoder gave the deployment angle to one arc min resolution. The geometric alignment was used to transfer the aspect solution to the sensor field-of-view, then the data from the infrared radiometer was used to obtain the final aspect values.



Backup was provided as a contingency in case one or more of the aspect devices failed. If the star tracker did not acquire a star or maintain the stellar reference, the ACS would have performed the attitude control program under inertial guidance only. The ACS position and rate readouts provided lower accuracy backup for the star mapper. Finally, a precision linear potentiometer mounted on the gimbal shaft was redundant with the optical shaft encoder.

In the sections that follow, details of the geometric reference measurements will be given as well as the techniques used to dynamically balance the payload. A complete development of the calculations which led to the azimuthal solutions will be described and results from the actual flights will be presented. Finally, a general approach to aspect solution through the star mapper, three axis position gyroscope readouts and/or a constrained axis of rotation will be formulated.

## 2. GEOMETRIC REFERENCE

An accurate geometric relationship was established before each flight between the infrared telescope, star tracker and stellar aspect sensor. These three optical sensors were mounted in a rigid, single piece, magnesium alloy, payload casting. Figure 1 shows the radiometer and star mapper mounted in the casting. Figure 2 is a diagram of the payload configuration and shows the relative location of the sensors more clearly.

The geometric measurements were made with the payload carefully mated to a precisely machined fixture which, in turn, was mounted onto a rotary table. The original reference for the fixture was obtained by leveling it to  $\pm 0.0001$  in. with a master precision level and centering it onto the rotation axis of the rotary table to within  $\pm 0.001$  in. by means of a "last word" dial indicator. Two precision levels were permanently installed orthogonal to each other on the receptacle plate and were used as the alignment references for all subsequent measurements once they were referenced to the master level.

The first aspect device to be aligned and calibrated was the star mapper. This instrument was designed and built at the Air Force Geophysics Laboratory and consisted of a Nikon 1:1.4 lens with a "N" slit reticle mask at the focal plane and a Fabrey field lens to focus the entrance pupil onto a ruggedized S-11 Bialkali photomultiplier. The reticle is a blackened electroformed nickel on copper plate through which three slits in the shape of an "N" has been etched with the outer legs made as parallel as mechanically possible. The 7.5 arc min width of the reticle slits were sized to give ten data samples per star crossing at the nominal survey roll rate. The legs of the "N" were separated by 7.75 degrees in azimuth and spanned 21 degrees in zenith angle. The reticle was positioned such that the first

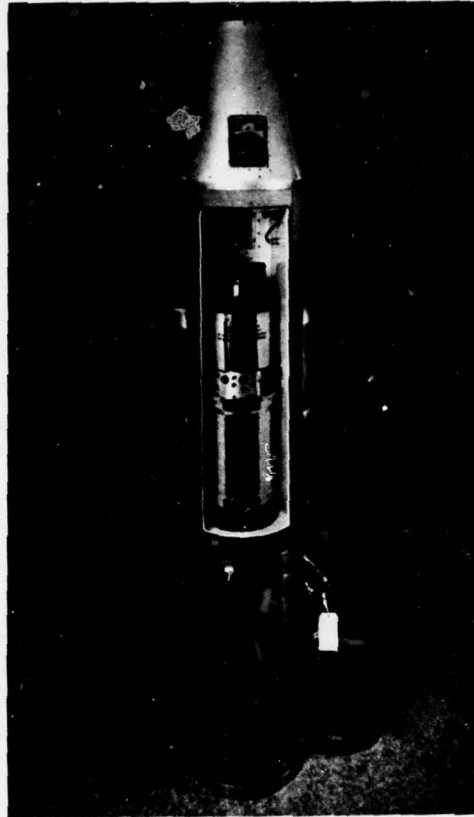


Figure 1. Payload Showing the Infrared Telescope in the Stowed Position. The star mapper may be seen above it

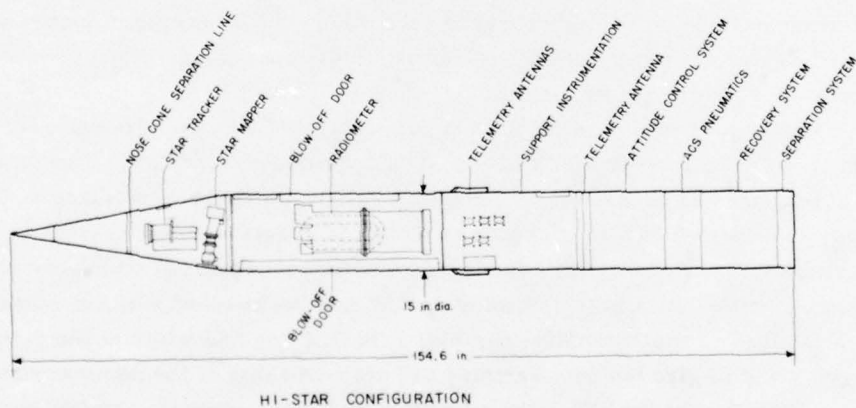


Figure 2. The Payload Diagram. The locations of the star tracker, star mapper and infrared telescope are shown

leg of the "N" was on the optical axis of the lens. Stars as faint as  $M_{S-11} \sim +4$  were easily detectable during the flights. The mapper was attached and pinned into the payload with the optical axis of the instrument elevated 10 degrees above the azimuth plane and the leading edge of the first leg of the "N" in the nominal deployment plane of the infrared telescope. A theodolite was set up and leveled to establish the azimuthal, or horizontal, reference plane of the payload. The photomultiplier was removed and the focal plane reticle backlit to make the slit edges easily visible in the theodolite. The payload was rotated and the rotary table angles were read when each of the slit edges were centered in the theodolite. The leading edge of the first slit was adopted to be the azimuth zero point reference. The theodolite elevation angle was depressed by about 1 degree and a new set readings taken on the rotary table angles of the slit edges. The theodolite was again depressed and the slit edge angles read; the procedure was repeated until the entire focal plane mask was mapped. In this manner the slit edges are measured as a function of zenith angle, that is, the complement of the theodolite depression angle. The measurements thus included the effects of lens distortion and cosecant zenith angle effects.

A least squares polynomial fit of the measured payload azimuth, minus the azimuth reference angle, against zenith angle was determined in order to functionally represent the slit edges; a parabola was used for the legs of the "N" while a cubic was required for the diagonal edges. The lens distortions were small for the lenses chosen for these experiments, the second and third order polynomials required for the fit arise from the cosecant zenith angle distortion of the measurements, and the series expansion representation of the tangent of the measured angles. Typical root mean square deviation of the curve fits ranged between 9 and 16 arc sec with the larger deviations occurring at the outer edges of the lens where the lens and cosecant zenith angle distortion were significant. Higher order curve fits were tried but did not significantly improve the accuracy. Figure 3 is a plot of the measured position of the slit edges and the resulting curve fits through them for one of the star mappers used on the survey. The lens distortion and cosecant effects are apparent as an increase in angular separation with decreasing zenith angle.

If the pole of rotation of the experiment were orthogonal to the azimuth plane, then mapping the stellar aspect sensor in this manner produced the same angular differences between slits as that measured for stellar transits. As seen from Figure 3, the "N" slit produces a unique pulse pattern which depends on the transit elevation of the star. When the pole of rotation is known the star mapper can be used as a transit instrument to provide the experiment azimuth as a function of time.



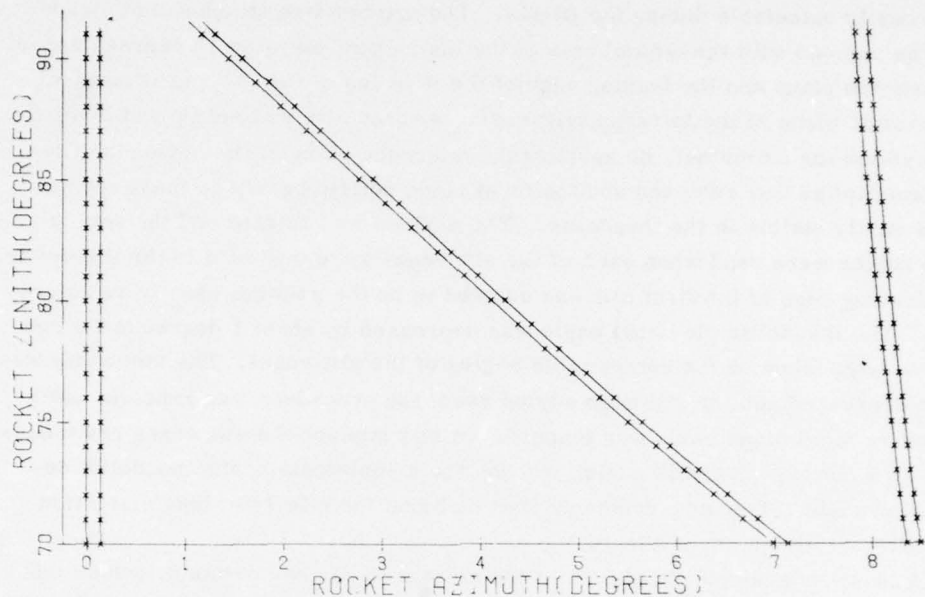


Figure 3. A Map of the "N" Slit Reticle for a Star Mapper Used on One of the Survey Flights. The increasing slit separation with decreasing zenith angle is due to the cosecant zenith angle and lens distortion

The star tracker was next mounted on top of the payload casting with the optical axis roughly co-aligned with the longitudinal, or roll, axis of the payload. The major elements of this sensor consisted of an image dissector with an S-20 photo-response and a 9 cm diameter lens. This instrument provides position information during flight to the attitude control system in the two axes orthogonal to its optical axis, that is, pitch and yaw. The error signals were used by the attitude control system to precisely null the roll axis to the inertial reference defined by the star to which the star tracker has been locked.

A synthetic star was built at AFGL to provide the proper optical input into the tracker during alignment. This star is a "point" source which has been filtered to simulate the optical energy distribution from an AOV star. The total output of the source can be adjusted to simulate the magnitude of the star selected for each experiment. This latter feature was important as the star tracker null position depended somewhat on source brightness.

The synthetic star was positioned to shine precisely along the rotation axis of the payload. The payload was then rotated and the tracker misalignments appeared as sinusoidal variations in the pitch and yaw axis. Position misalignments between

the rotation axis of the casting and the star tracker null were corrected by adjusting the tracker error potentiometers if the errors were less than 2 arc min. Larger misalignments were corrected by shimming the tracker then nulling the potentiometers.

Calibration of the infrared telescope deployment was done last. The azimuth reference of the leading edge of the first slit of the star mapper was re-established with the theodolite. The infrared sensor was mounted into the gimbals, then deployed to various zenith angles within the projected limits of the survey scan. At each deployment position the rotary table and theodolite depression angles were adjusted until the sensor reference, a fiducial mark etched onto the center of the focal plane array, was centered in the theodolite as viewed through the telescope optics. At each deployment position the sensor zenith angle, measured as the complement of the theodolite depression, and sensor azimuth bias angle were recorded as dependent variables of the 13 bit optical shaft encoder output and the precision linear potentiometer readout. The deployment bias angle was taken as the azimuth difference between the sensor azimuth angle and the azimuth reference point.

The sensor deployment calibration equation was determined by means of a linear regression fit of the observed zenith angles against the shaft encoder readout and, independently, the position potentiometer. The shaft encoder was geared to give a 1 arc min digitization uncertainty while the potentiometer outputs had about half that measurement accuracy. The least squares curve fit of the deployment angle versus shaft encoder readout was good to one to 1.25 arc min rms, the same size as the digitization uncertainty. The azimuth biases were of the order of 20 arc min, or less, and were represented by a parabolic fit through the measurements as a function of zenith angle.

### 3. DYNAMIC ALIGNMENT

The experiment design required the geometric roll axis of the payload to be fixed to an inertial reference by maintaining lock of the star tracker to a selected star while the payload was rotated about this axis. In order to insure that the attitude control system would be able to maintain the inertial reference during this rotation, the cross products of inertia in the orthogonal axes had to be reduced by dynamically balancing the payload.

The dynamic alignment of the experiment was done on a spin balancing machine originally developed under the direction of Mr. Russ Nidey for the Kitt Peak National Observatory and subsequently transferred to AFGL. The machine was composed principally of two air bearings, a spherical bearing mounted on top of a

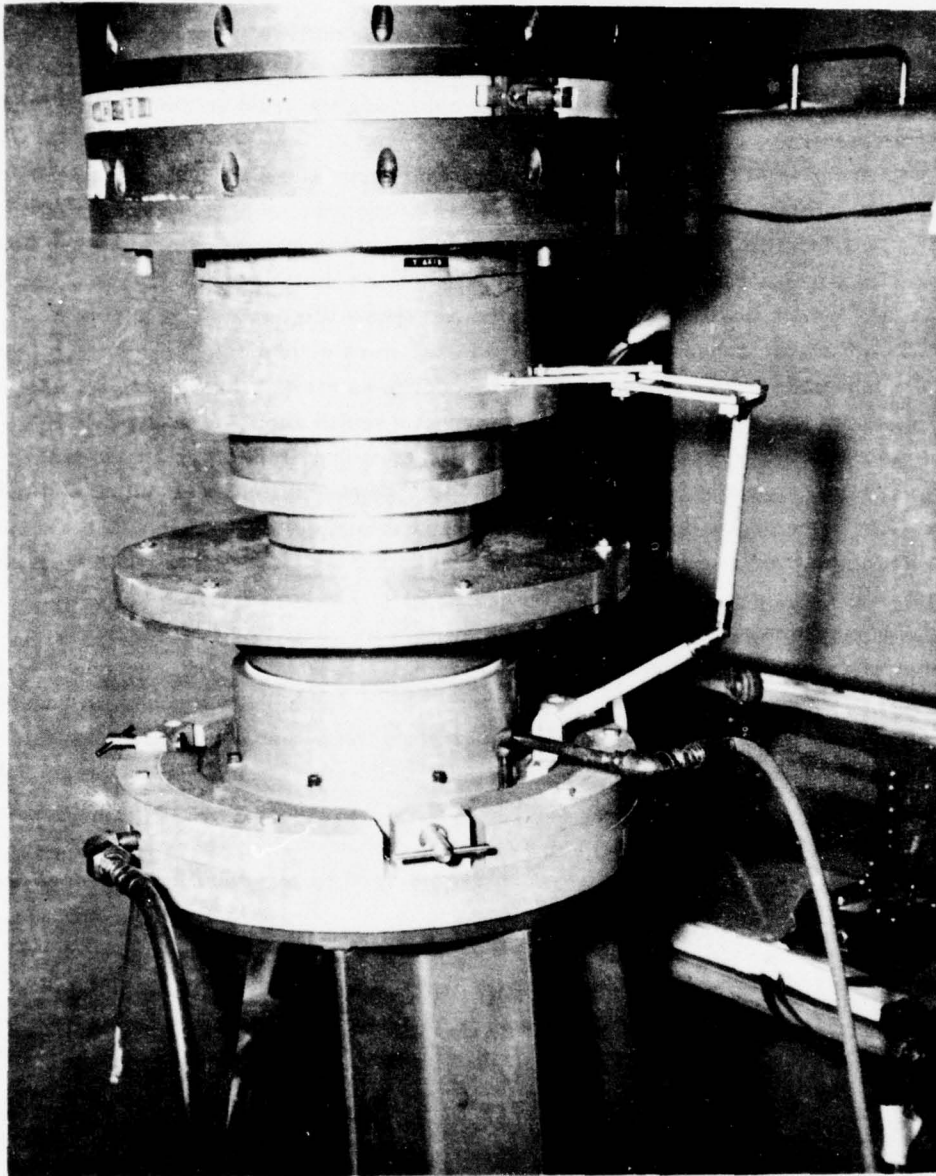


Figure 4. Payload Mounted on the Dynamic Balancer. The hoses are air lines to the air bearings. The flat air bearing used for translational motion is at the bottom of the fixture. The spherical air bearing, which allows rotational motion may be seen in the lower center of the fixture



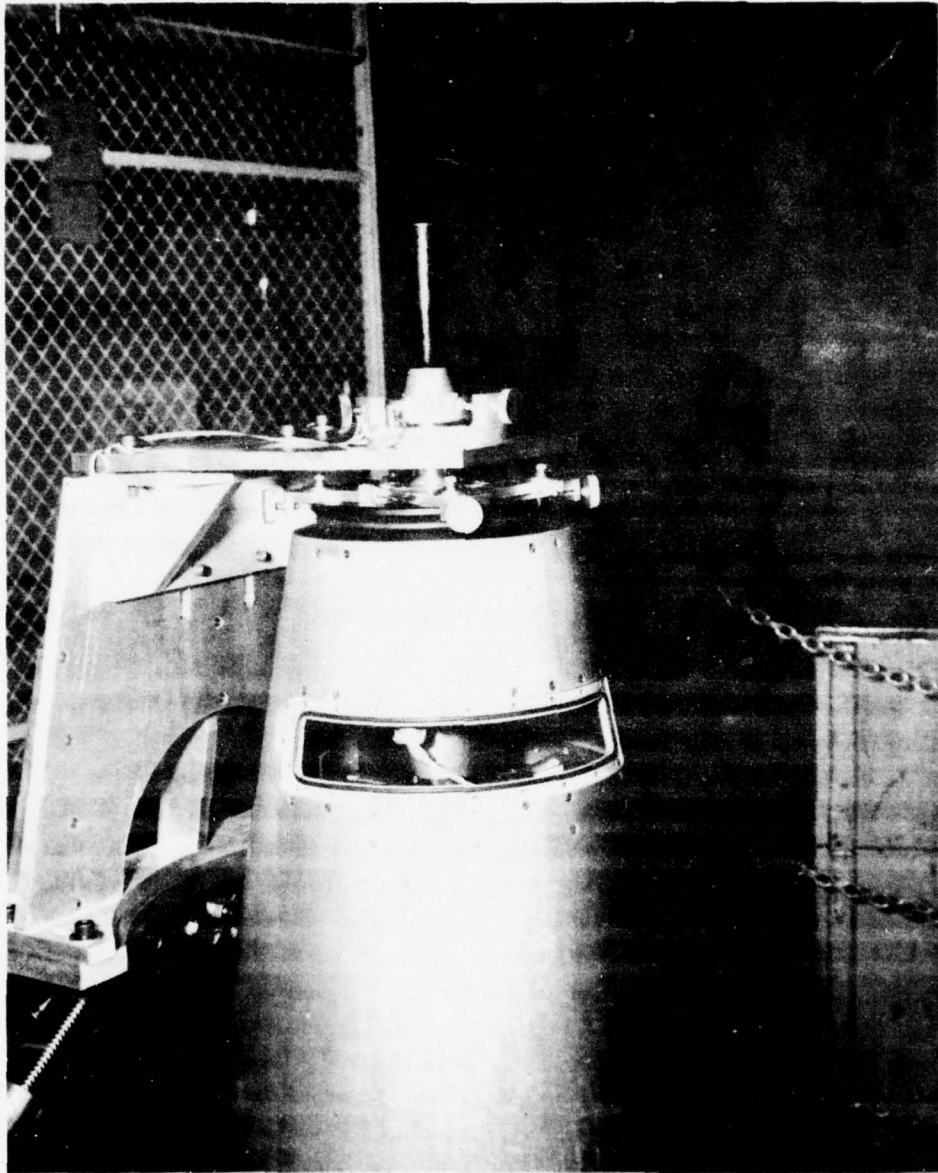


Figure 5. The Constraining Fixture for the Balancer. The payload on the balance is prevented from tipping over by a fixture which limits the travel of the top end of the payload. Also seen are the two precision levels mounted in the payload which are used for the initial static balance



flat plate bearing. The flat plate air bearing allows translational motion while the spherical bearing permits rotational freedom. Two rate gyroscopes on the spherical air bearing sensed pitch and yaw rates.

The payload was assembled and mounted on the spin balancer as shown in Figure 4. The nose cone, star mapper and sensor payload doors were removed and the infrared sensor was deployed to a zenith angle midway between the projected scan limits. Thus, the payload configuration closely simulated that of the data taking portion of the experiment. The movement of the top of the payload was limited by a rig, as seen in Figure 5. A drive motor mounted on the spherical air bearing spun the payload at two revolutions per second, and the gyroscopes read the pitch and yaw rates as the spinning payload tipped off of vertical. The balancer was stopped and weights were taped to the outside of the payload. The size and location of the weights were estimated from the rates measured by the gyroscopes. The payload was again spun up, the tip off rates remeasured, and new sizes and locations determined for the weights. About 100 to 150 iterations over a two to three day period were required before the cross moments were brought within acceptable limits.

After balancing, the payload was taken off the balancer and the weights were anchored inside the payload.

#### 4. EXPERIMENTAL PROFILE

After the optical alignment and functional systems checks at AFGL, the payload was packed and shipped to the launch site. The instrument support, attitude control and recovery sections were attached to the experiment casting section by means of countersunk screws driven into tapered screw holes at constant torque. These sections were attached with the aid of a "last word" indicator in order to maintain the geometric roll axis defined by the payload casting. After the payload was dynamically balanced, the casting was separated and the star mapper and infrared telescope deployment calibrations were checked. The casting was re-attached to the other sections and the entire payload was cleaned under class 100 clean room conditions.<sup>4</sup> The payload was then mated with the rocket and placed into the launch tower.

The ACS provided three axis control of the payload through inertial references on a roll stabilized platform. Position and rate readouts were provided in the pitch, roll and yaw axes. ALRC provided a calibration of these readouts. The offset

4. Price, S.D., Cunniff, C.V., and Walker, R.G. (1978) Cleanliness Considerations for the AFGL Infrared Celestial Survey Experiments, AFGL-TR-78-0171.

between the north point reference of the ACS and geographic north was measured while the rocket was in the launch tower. Typical offsets were on the order of three arc min.

The declinations of the "pole" stars selected for the inertial references were all within 9 degrees of the latitude of the launch site (all but one star was within 6 degrees). The rocket was launched about 4 min before meridian transit of the star in order for the payload pole of rotation to be at maximum elevation during data gathering. Thus, the rotation pole was not more than 9 degrees off the local zenith.

During rocket burn, the vehicle attitude was spin stabilized with a one and a half revolution per second spin. After powered flight, the vehicle coasted until the aerodynamic forces were reduced enough so that the ACS could control the payload attitude. The nose cone, star mapper and sensor housing doors were ejected while residual drag was still present so that aerodynamic and centrifugal forces from the payload spin, carried these objects away and below the payload. The vehicle was despun with the release of yo-yo weights, then separated from the sustainer by release of a Marmon clamp. The springs used to separate the payload were sized for a separation velocity of 2 m per second.

The attitude control system pointed the star tracker to within 2 degrees of the "pole" star. The tracker had an 8 degree field-of-view and was designed to acquire the brightest source in this field. Once star presence was noted, acquisition was obtained from the tracker pitch and yaw error signal, driving the ACS to center the star to tracker null. Once null had been obtained the tracker was switched to fine control which reduced the tracker field-of-view to  $\pm 2$  arc min in both axes with the deadband at 20 arc secs.

The infrared sensor was then deployed to the minimum zenith angle (about 38 degrees) and the payload spun up about the roll axis. The sensor was stepped down 1.1 degrees (slightly less than the 1.2 degree total field-of-view of the instrument) under the command of a turn pulse generated by the attitude control system when it sensed that the payload reference was nominally at  $350^\circ$  azimuth. In this manner a contiguous sector of the sky was swept out. A graphical depiction of the survey scan pattern is seen in Figure 6.

Once the payload was accelerated the roll jets were disabled for much of the survey scanning. However, the effective linear scan rate of the sensor did change as the sensor stepped under constant roll rate. To correct for this cosecant zenith angle change in linear scan rate, three roll rate changes were incorporated into the ACS which were programmed to occur at the beginning of specified rolls, that is at specific deployment angles. The rate changes were sized such that, barring secular perturbations, the effective linear scan rate of the sensor was to be maintained between the design value and 15 percent over.

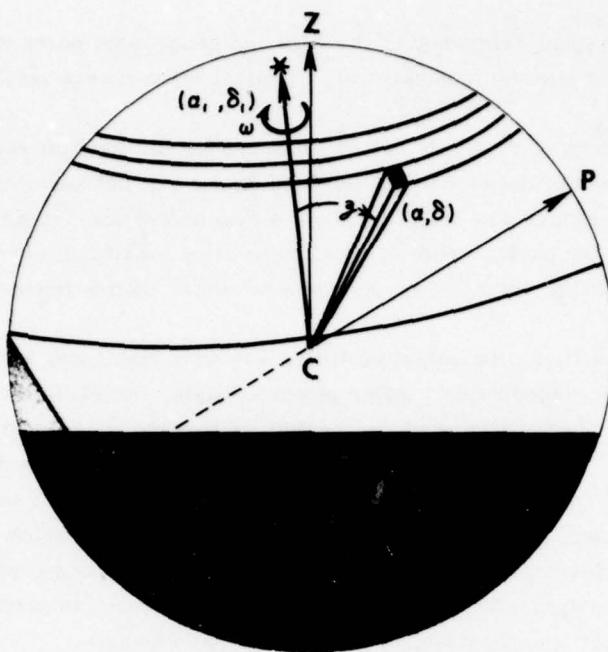


Figure 6. Experimental Geometry. The star tracker locks to a star with celestial coordinates  $\alpha$  and  $\delta$  near local zenith,  $z$ . The payload is spun at an angular rate,  $\omega$ , and the telescope deployed to a zenith angle,  $z$ . After completion of a  $360^\circ$  roll maneuver the zenith angle is increased slightly less than the field-of-view of the telescope. Thus, a series of rolls sweep out a contiguous sector of the between the maximum and minimum zenith angle for the experiment

Small secular accelerations amounting to 0.05 to one percent of the roll rate were observed during the survey as the energy expended to maintain lock onto the star cross coupled into the roll motion. The misalignment between the tracker electronic null which defined the geometric roll axis and the longitudinal principal moment of inertia was time dependent and arose from the residual cross products of inertia not corrected for by spin balancing, the changing distribution of mass due to sensor stepping and the expenditure of helium by the sensor and nitrogen by the attitude control system. The imbalance due to sensor stepping was probably the most important effect as a roll rate change of 10 percent was observed at the end of each flight as the sensor was stowed from the fully deployed position. These small misalignments caused the star to be positioned at the edge of the star tracker deadband in a constant orientation in the tracker pitch-yaw plane.



At the end of the experiment the sensor was stowed and the payload recovered. The flight instrumentation was refurbished and reflown. Seven experiments were launched out of White Sands Missile Range, latitude 32.5 degrees North, and three more from the Weapons Test Establishment, Woomera, Australia, latitude 32 degrees South.

## 5. AZIMUTH ASPECT

An azimuth, zenith distance coordinate system was established for the experiment through the geometric alignment. The pole of rotation was inertially fixed by the star tracker to the celestial coordinates of the selected "pole" star and the azimuth reference was defined by the leading edge of the first reticle slit of the star mapper at 90 degrees zenith distance. The azimuth aspect was determined as a polynomial representation of the reference point azimuth as a function of time through a least squares calculation of the observed star mapper crossings.

Fixing the rotation axis to a known set of coordinates permitted an "a priori" calculation of the stars to be scanned by the star mapper and, through the geometric calibration, the anticipated pulse pattern. The positions of the 300 brightest stars which had S-11 photoresponse magnitudes brighter than +4 were precessed to the epoch of each experiment and rotated into the azimuth-zenith distance coordinates of the payload. The stars were then sorted in order of increasing azimuth and limited to those stars contained in a zenith distance band defined by the limits of the star mapper. The bright planets were also included if their positions at epoch, obtained from the "American Ephemeris and Nautical Almanac," placed them in the scan pattern.

The predicted pulse pattern of voltage as a function of reference point azimuth was calculated by convolving the star mapper reticle calibration equations with the stellar position and magnitude data. Referring to Figure 3 it is apparent that each star transit of the mapper produces three pulses and that the azimuth of the second pulse with respect to the first and last is a unique function of the zenith distance if the geometric and rotation poles are coincident. The pulses were identified by the Bright Star<sup>5</sup> number of the transited star plus a designator for the slit through which the star is observed. A data list was then generated which contained the reference azimuth, S-11 magnitude and identifier of the pulses in the predicted pattern ordered by increasing azimuth.

A segment of the predicted pulse pattern for one of the experiments may be seen at the top of Figure 7. The ordinate is the reference azimuth and the abscissa,

---

5. Hoffleit, D. (1964) Catalog of Bright Stars, 3rd Edition, Yale University Observatory.

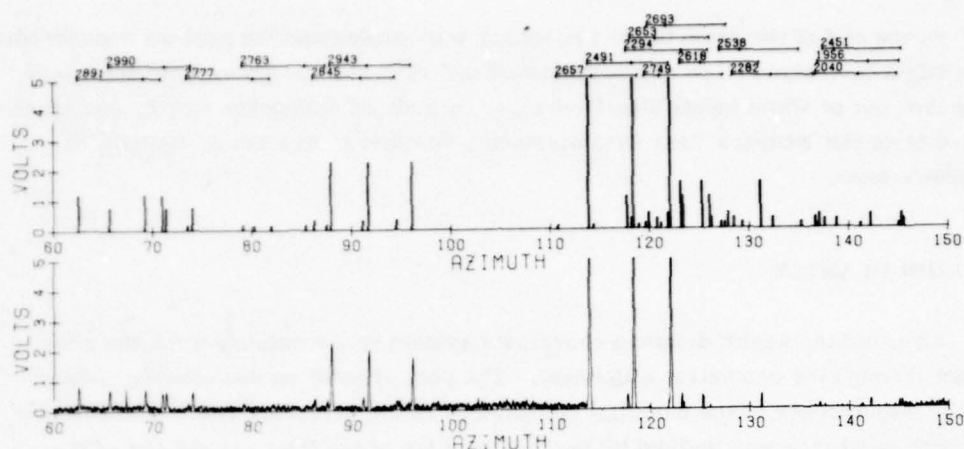


Figure 7. Comparison Between the Calculated Output of the Star Mapper and the Observed. The calculated output is shown at the top of the figure after the final aspect solution has been obtained and the actual output is at the bottom. The Bright Star number of the star producing the triad of pulses is given at the very top of the diagram and the tick marks locate the position of individual pulses

the anticipated output voltage. The bright star number of the transiting source is given above the triad of pulses it produces and is more clearly delineated with the tick marks. The observed star mapper output, after the aspect has been solved for, is shown at the bottom of Figure 6.

The star mapper data was reduced to obtain the time and amplitude of the observed star pulses. A pulse was selected with the criterion that a number of consecutive data samples, corresponding to the transit time of a slit, were above a specified amount greater than the running value of the calculated noise. The exact value of the acceptance level was empirically determined for each flight. This procedure was used instead of a signal to noise criterion because the data were non-linear. The star mapper electronics were ac coupled in order to filter out the baseline wanderings due to extended phenomenon such as emission from the galactic and ecliptic planes and off axis radiation from the moon or OH layer of the earth's atmosphere. Consequently, the undershoot due to bright sources drives the voltages negative and the telemetry clipped the output at zero volts. An example of this is shown in the bottom of Figure 6 following the pulses due to BS 2491.

A peak amplitude and time of peak for each of the potential sources were obtained by curve fitting a parabola through the data points near peak and calculating these quantities from the curve. For saturated pulses the peak was assumed to occur at the midpoint of saturation. The pulse data were divided into blocks corresponding to separate rolls, and delineated by the times of the turn pulses sent by

the attitude control system when it sensed the completion of a  $360^\circ$  roll. These turn pulses initiated stepping of the sensor. Four of the rolls were further divided into segments which were actively accelerated by the roll jets, that is, the initial spinup of the payload and the three roll rate changes, and "unperturbed" segments. Taking the data in blocks corresponding to rolls was a natural division since the same predicted pulse pattern applies to each one of the rolls.

The sought for aspect solution for each roll was a second or third order polynomial which converted the times of the observed pulses into azimuths such that the deviations between the observed and predicted pulse pattern were minimized in the least squares sense.

The initial step was to select a prominent pulse, common to all rolls, from the list of observed pulses and to identify it in the predicted output data file. This pulse was usually, but not always, the first slit transit of the brightest star. Successive identical pulses occurred after exactly a  $360^\circ$  degree roll was completed. Since the azimuth of the pulse was known and the times of occurrence were measured an initial aspect solution was obtained by assuming a constant roll rate between the pulses. The azimuth aspect solution then was expressed by

$$Az_n(t) = A(*) + 360^\circ * \frac{t - t_n(*)}{t_{n+1}(*) - t_n(*)}, \quad t_{na} \leq t \leq t_{nb} \quad (1)$$

where  $Az_n(t)$  is the aspect azimuth solution for the  $n^{th}$  roll,  $A(*)$  is the azimuth of the pulse,  $t_n(*)$  and  $t_{n+1}(*)$  are the pulse times on the  $n^{th}$  and  $(n + 1)$  roll respectively, and the time,  $t$ , is limited to values between the beginning of the  $n^{th}$  roll,  $t_{na}$ , and the end,  $t_{nb}$ .

This initial aspect solution for the  $n^{th}$  roll was used to convert the observed pulse times into azimuths. The predicted and observed pulses were compared and each observation was assigned the designation and azimuth of the nearest predicted pulse and a weight equal to the observed voltage. A weighted least squares regression of azimuth as a function of time was calculated with the order of the polynomial of the regression fixed.

The energy from the fine pitch and yaw jets used to correct for the small misalignment between the dynamic and geometric roll axis cross coupled to the roll motion. Each activation of a jet produced a small change in rate and the jet firings were more or less uniformly timed during a roll such that the pole star was offset at about 20 arc sec from the star tracker null in a constant body fixed pitch and yaw direction. It was therefore assumed that the jets produced a constant secular acceleration in roll rate during the course of a roll. Different rolls had different accelerations as sensor stepping changed the cross moments of inertia. A parabolic



regression, that is, constant acceleration, was found to give an excellent aspect solution for almost all of the rolls. A cubic was required for the last rolls on one experiment where a small amount of aerodynamic force could have perturbed the dynamics.

The differences between the assigned and calculated azimuths were examined. If all the differences were within 3 arc min, the solution was accepted as final. Otherwise, the weight of the pulse with the largest deviation was set to zero and a new weighted regression was calculated. The deviations of the new regression were checked and the weight of the pulse with the largest deviation was zeroed and new regressions calculated. This procedure was iterated until the absolute value of the largest deviation was less than 3 arc min. A new set of azimuths were calculated for the pulses given zero weight. These azimuths were compared with the predicted pattern to check if there were any changes in the predicted pulses which were close to the zero weighted pulses. If such changes did occur, then the original weights of the pulses were restored and the new designations and azimuths of the closest predicted pulses were assigned to them. If there were no reassignment of designation and azimuth, then all the adjustments were made that could be and the current aspect solution was accepted as final. If one or more of the observed pulses was reassigned a designation and azimuth, then a new weighted regression was calculated, the largest deviation greater than an absolute value of 3 arc min was assigned a zero weight and the entire process is repeated until (a) no reassignment of designation or azimuth occurs at that step of the procedure or (b) the absolute value of the largest deviation from the first regression curve calculated after the designation and azimuth reassignment is less than 3 arc min. If the initial aspect solution was not accurate enough to correctly assign designations and azimuths to a sufficient number of pulses, the solution could diverge. In this case, the procedure is stopped after 50 iterations and a closer examination of the initial aspect was required. Typical root mean square values of the deviations from the final aspect solutions for the "unperturbed" rolls were 1 to 1.5 arc min. These errors may well have been dominated by the uncertainties in determining the location of the pulse peak since they are roughly the size which corresponds to the telemetry sample time.

The next step was to find aspect solutions for the roll segments which include the initial spinup of the payload and the three periods of rate changes. As before, the observed list was searched for prominent pulses, except that for these rolls one or more pulses were identified and a permanent weight of 5, which corresponds to the maximum telemetry output, given to them. An initial roll rate and rate change for these roll segments were obtained from either a linear regression of the ACS roll rate telemetry output or a linear interpolation between the beginning and ending roll rates determined by the aspect solution for the unperturbed rolls on



either side of the roll segment in question. This rate equation was integrated to give the initial aspect as a quadratic function of time with the reference azimuth and time set equal to the identified pulse (or one of them). An iterative procedure similar to the one used for the unperturbed rolls was used for the azimuth solution except that the pulses which were initially identified were not allowed to be assigned a zero weight. Except for a few of these perturbed roll segment which had only a very limited number of observed pulses, the rms errors of the final aspect solutions were comparable to those obtained on the unperturbed rolls.

As noted earlier, with the payload roll and geometric axis fixed to a known set of inertial coordinates the star mapper may be considered as a transit instrument. The advantage of this configuration is that attitude control system rate outputs can be calibrated and updated through the star mapper pulses. Aspect determination in just such a manner was required for the fourth of the White Sands series of flights. During the powered portion of this flight one of the dynodes of the photomultiplier opened up, reducing the sensitivity to such an extent that only Bright Star 2326 ( $\alpha$  Car) and Venus were detected. Thus, an insufficient number of pulses were observed to permit the calculation of an adequate solution by the previously described procedures.

An aspect solution was obtained by integrating the roll rate equation calculated from the output of the roll rate gyroscope and determining the azimuth zero points and gyroscope drift and calibration errors with the star pulse observations. The rate rather than position readouts were used because of the smaller gyroscope drift and the better signal to noise due to the large telemetry scale allocated to the rate gyroscopes.

The telemetry conditioned output of the roll rate gyroscope was converted to an angular rate by means of the calibration equation supplied by ALRC before the flight. As before, the data is divided into blocks of rolls defined by the turn pulse times, plus the four roll segments with roll rate changes. A linear least squares regression of the ACS roll rate as a function of time was calculated for each roll. These solutions differed from the true roll rate due to (a) errors in the constants used to convert the telemetry output into roll rate and (b) drift in the roll rate gyroscope. Since the roll rate calibration equation was linear with respect to the output and it was assumed that the gyroscope drift was constant with time, the true roll rate ( $\omega_T$ ) was given by

$$\omega_T(t) = \gamma \omega_{ACS}(t) + \delta \quad (2)$$

where  $\omega_{ACS}(t)$  is the ACS roll rate output and  $\gamma$  and  $\delta$  are the necessary correction factors. For the  $j^{th}$  roll the ACS roll rate was given by

$$\omega_{ACS}(t) = \omega_j + \omega_j' t \quad (3)$$

The azimuth aspect solution is obtained by integrating Eq. (3)

$$\int_{A_j}^A dA' = \int_{t_j}^t \omega_{ACS}(t) dt = \int_{t_j}^t (\omega_j + \omega_j' t) dt \quad (4)$$

$$A - A_j = \omega_j (t - t_j) + \frac{\omega_j'}{2} (t^2 - t_j^2)$$

here  $t_j$  and  $A_j$  are the beginning time and azimuth respectively, for the  $j^{\text{th}}$  roll. If there were no gyroscope drifts and the ACS telemetry calibration equation for the roll rate were exact, then the azimuth and times of pulses could be used to calculate a mean value of  $A_j$ , the only unknown in Eq. (4). The true azimuth solution is given by

$$\int_{Az_j}^{Az} dAz' = \int_{t_j}^t \omega_T dt = \int_{t_j}^t [\gamma(\omega_j + \omega_j' t) + \delta] dt \quad (5)$$

$$Az - Az_j = (\gamma\omega_j + \delta)(t - t_j) + \frac{\gamma\omega_j'}{2} (t^2 - t_j^2)$$

Combining Eqs. (4) and (5)

$$(Az - Az_j) - (A - A_j) = (\gamma - 1) \left[ \omega_j (t - t_j) + \frac{\omega_j'}{2} (t^2 - t_j^2) \right] + \delta(t - t_j) \quad (6)$$

$$Az - \omega_j(t - t_j) + \frac{\omega_j'}{2} (t^2 - t_j^2) = Az_j + [(\gamma - 1)\omega_j + \delta](t - t_j) + (\gamma - 1) \frac{\omega_j'}{2} (t^2 - t_j^2) \quad (7)$$

Here all the quantities on the left hand side of Eq. (7) are known for a star pulse and a number of observed pulses can be used to obtain a best fit through a three variable regression for the azimuth,  $Az_j$  and the coefficients of  $(t - t_j)$ ,  $(t^2 - t_j^2)$  with the values of  $\gamma$  and  $\delta$  following directly from these coefficients. Unfortunately,

$$\omega_{ACS}(t) = \omega_j + \omega_j' t \quad (3)$$

The azimuth aspect solution is obtained by integrating Eq. (3)

$$\int_{A_j}^A dA' = \int_{t_j}^t \omega_{ACS}(t) dt = \int_{t_j}^t (\omega_j + \omega_j' t) dt \quad (4)$$

$$A - A_j = \omega_j (t - t_j) + \frac{\omega_j'}{2} (t^2 - t_j^2)$$

here  $t_j$  and  $A_j$  are the beginning time and azimuth respectively, for the  $j^{\text{th}}$  roll. If there were no gyroscope drifts and the ACS telemetry calibration equation for the roll rate were exact, then the azimuth and times of pulses could be used to calculate a mean value of  $A_j$ , the only unknown in Eq. (4). The true azimuth solution is given by

$$\int_{Az_j}^{Az} dAz' = \int_{t_j}^t \omega_T dt = \int_{t_j}^t [\gamma(\omega_j + \omega_j' t) + \delta] dt \quad (5)$$

$$Az - Az_j = (\gamma\omega_j + \delta)(t - t_j) + \frac{\gamma\omega_j'}{2} (t^2 - t_j^2)$$

Combining Eqs. (4) and (5)

$$(Az - Az_j) - (A - A_j) = (\gamma - 1) \left[ \omega_j (t - t_j) + \frac{\omega_j'}{2} (t^2 - t_j^2) \right] + \delta(t - t_j) \quad (6)$$

$$Az - \omega_j(t - t_j) + \frac{\omega_j'}{2} (t^2 - t_j^2) = Az_j + [(\gamma - 1)\omega_j + \delta](t - t_j) + (\gamma - 1) \frac{\omega_j'}{2} (t^2 - t_j^2) \quad (7)$$

Here all the quantities on the left hand side of Eq. (7) are known for a star pulse and a number of observed pulses can be used to obtain a best fit through a three variable regression for the azimuth,  $Az_j$  and the coefficients of  $(t - t_j)$ ,  $(t^2 - t_j^2)$  with the values of  $\gamma$  and  $\delta$  following directly from these coefficients. Unfortunately,

the 4 to 6 pulses observed for each roll were not enough to produce a stable solution. The reason for this can be seen from Eq. (7). With  $\gamma$  close to 1.0,  $(\gamma - 1)$  is a small quantity as is  $\omega_j$ , thus the statistical uncertainty resulting from too few data points has a profound effect on determining  $\gamma$ . Since  $\gamma$  and  $\delta$  are coupled in the  $(t - t_j)$  coefficient through the comparatively large  $\omega_j$ , a small error in  $\gamma$  results in a large error in  $\delta$ .

To constrain the solution to realistic values,  $\gamma$  was assumed to be a known constant whose value is approximately 1. Equation (1) is solved by least squares procedures to obtain  $Az_j$  and  $\delta$  for each roll. There are enough observed data points to give significant results under these conditions. Since it was assumed that the roll rate gyroscope drift term is constant and that the roll rate is a linear function of time,  $\gamma$  and  $\delta$  are constant for the entire flight, that is, both effects are linear in time and  $\gamma$  and  $\delta$  adjust the observed linear values to the correct ones. However, an incorrect choice of  $\gamma$  for Eq. (7) will produce a time dependent value of  $\gamma$  as may be seen by rewriting the time dependent part of Eq. (7).

$$[(\gamma - 1)\omega_j + \delta](t - t_j) + (\gamma - 1)\frac{\omega_j}{2}(t^2 - t_j^2) = \left[(\gamma - 1)\left(\omega_j + \frac{\omega_j}{2}(t + t_j)\right) + \delta\right](t - t_j) .$$

The azimuth aspect was iterated by varying the value of  $\gamma$  until  $\delta$  was a constant for all rolls. Specifically, an initial value of 1.0 was assumed for  $\gamma$  and a least squares regression of Eq. (7) with the observed pulse azimuth and time of peak to obtain  $Az_j$  and  $\delta$  for each roll. The roll to roll trend, and hence time dependence, found for  $\delta$  was used to estimate a new value of  $\gamma$ . This new value of  $\gamma$  was used to calculate a new aspect solution with updated values of  $Az_j$  and  $\delta$ . Six iterations of this procedure were required before  $\gamma$  was a constant for all rolls for the flight in question. The root mean square of the deviations for the final solutions were between 1.5 and 4.7 arc min, one to three times larger than the rms derived on other flights using the star mapper alone.

## 6. ASPECT UPDATES THROUGH THE INFRARED SENSOR

The aspect solutions obtained from the star mapper allows the calculation of the position of the aspect reference, which was nominally in the deployment plane of the infrared telescope, for anytime during the course of the experiment. The zenith angle and azimuth of the center of the infrared telescope defined by the fiducial mark on the focal plane was calculated from the deployment calibration and the optical shaft encoder output and adding the deployment bias angle to the aspect solution. The focal plane layout of the location of each detector with respect to the fiducial mark was used to transfer the aspect of the center of the field of view to the center of a detecting element which observed a potential source.



The positions of potential sources were compared on a roll by roll basis to objects contained in various lists of sources known, or suspected, to be bright in the infrared. Associations made between observed AFGL sources and objects in the 2.2 micron catalog, commonly referred to as the IRC, of Neugebauer and Leighton<sup>6</sup> were used to update the aspect of the infrared telescope. The IRC, and its unpublished extension,<sup>7</sup> contain positions and magnitudes for over 6000 sources brighter than +3 at 2.2 microns. Over 80 percent of the 4.2 microns survey sources were associated with IRC objects.

Positions in the IRC were improved by adopting more precise data from the Smithsonian Astrophysical Observatory Star Catalog<sup>8</sup> for those objects common to both catalogs. Those data were then precessed to the epoch of each experiment and rotated into the azimuth-zenith angle coordinate system of the payload and infrared telescope. The list of IRC objects was sorted in terms of increasing azimuth, then into blocks of objects contained in a band swept out by the sensor on each roll. An association was made with the closest IRC object to the potential source within  $\pm 4.5$  arc min in azimuth and  $\pm 0.105$  degrees in zenith angle. These values were empirically determined to give a good set of associations from the initial aspect solution and correspond to a detector width at minimum deployment and the half height of a detector plus one optical blur circle diameter at 20 microns.

Azimuth and zenith angle differences between the observed position of the source and the updated IRC position were calculated for each association and an average offset for each coordinate obtained for every roll. These offsets were added to the aspect solution for the rolls and a new set of associations and offsets calculated. This procedure was iterated until no new associations were found. A list of sources with IRC associations and large signal to noise was printed for each roll using the final offsets.

Each roll was then checked individually. The limits of association were narrowed to  $\pm 0.095$  degrees zenith and  $\pm 0.05$  degrees azimuth and a new set of position offsets determined with extra weight given to the associations of source is detected on adjacent rows of detectors. The uncertainty in the zenith angle of a source which transited the detector to detector overlap regions was about four times less than that in the non-overlapped region. A final set of bias angles in zenith angle and azimuth data were obtained, then applied to the data.

- 
6. Neugebauer, G., and Leighton, R.B. (1969) Two Micron Sky Survey, A Preliminary Catalog, NASA SP-3047.
  7. Neugebauer, G. (1971) Extension to the Two Micron Sky Survey, unpublished.
  8. Smithsonian Astrophysical Observatory (1966) Star Catalog, Smithsonian Publication 4652, U. S. Government Printing Office.

After the final aspect solution for the sensor output was derived an error corresponding to the half width at half maximum of the signal was assigned to the azimuth position and a detector half height to the zenith angle of the observation. The zenith angle error was reduced to the height of the overlap region if the source was detected on adjacent detectors. The position and the associated errors were transformed into celestial coordinates. The errors in right ascension and declination were taken as the unsigned, that is, absolute value, combination of the azimuth and zenith angle error in each celestial coordinate. Specifically:

$$\begin{aligned}\Delta\delta &= a_0 \Delta z + a_1 \Delta A \\ \Delta\alpha &= (a_1 \Delta z + a_0 \Delta A) / \cos \delta \\ a_0 &= |\cos \delta_p \cos z \cos A + \sin \delta_p \sin z| / \cos \delta \\ a_1 &= |\cos \delta_p \sin A / \cos \delta|\end{aligned}\tag{8}$$

where

$\Delta\alpha$ ,  $\Delta\delta$  are the errors in right ascension, at  $\alpha$ , and declination at  $\delta$ , respectively

$\Delta A$ ,  $\Delta z$  are the errors in azimuth, at  $A$ , and zenith angle, at  $z$ , respectively  
 $\delta_p$  is the declination of the pole star.

Note that an error box generated with  $\pm\Delta\alpha$  and  $\pm\Delta\delta$  around the observed position of the source at  $(\alpha, \delta)$  was larger than the original  $(\pm\Delta A, \pm\Delta z)$  error box.

Sources observed on two, or more, separate experiments were identified as the same object if these azimuth-zenith angle error boxes overlapped. The positions and brightnesses of these multiply observed objects were obtained from the means of the individual values. The positional error assigned to the source was the root sum square of the individual right ascension or declination error plus the sum square of the deviations of the individual positions from the mean, all divided by twice the total number of individual observations. Figures 8 and 9 are histograms of the right ascension errors, reduced to the equator, and declination errors determined in this manner for the source contained in the AFGL Four Color Infra-red Sky Survey of Price and Walker.<sup>2</sup> A bimodal distribution is apparent in both histograms. The peak of 3.8 arc min is due to the singly observed sources whereas, the multiple observations reduce the errors such that they peak at 2.2 arc min.

These errors are conservative estimates of the positional uncertainty of the source which arose not only from the error in the aspect determination but also

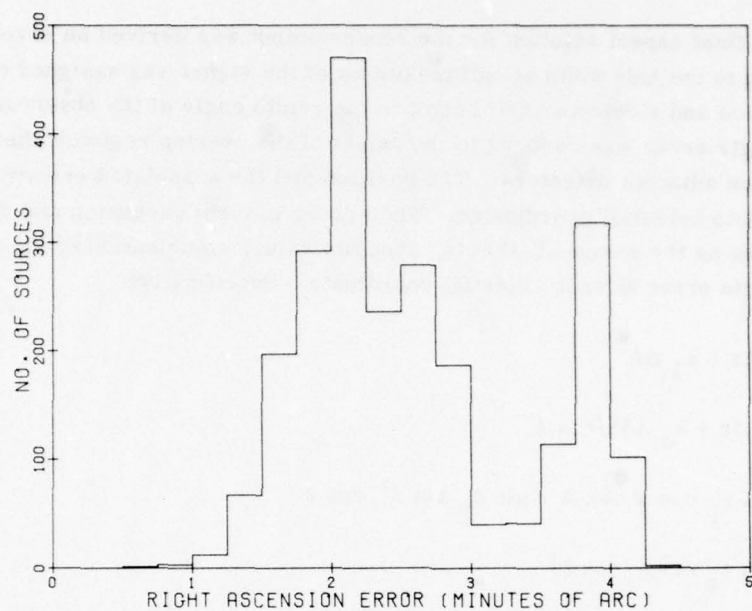


Figure 8. The Distribution in the Calculated Uncertainties of the Right Ascensions, Reduced to the Equator, of all the Sources in the AFGL Catalog.<sup>2</sup> The bimodal distribution arises from the difference in positional uncertainty between the singly and multiply observed sources

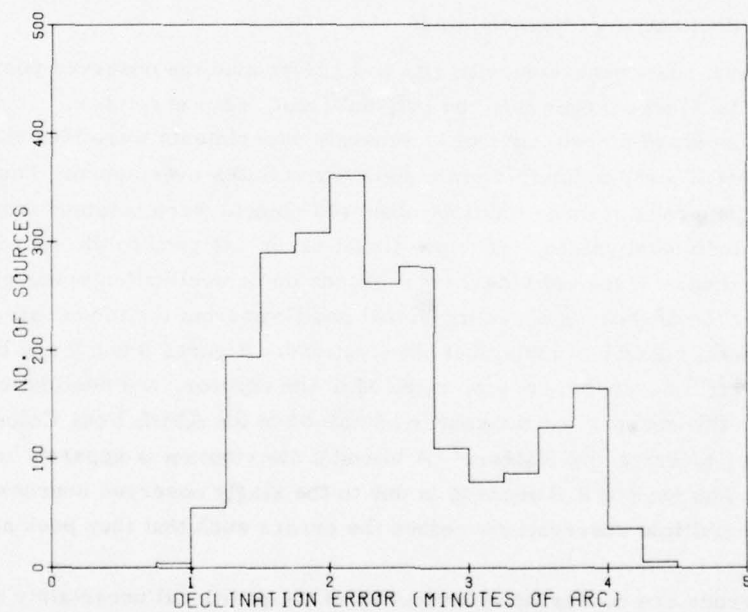
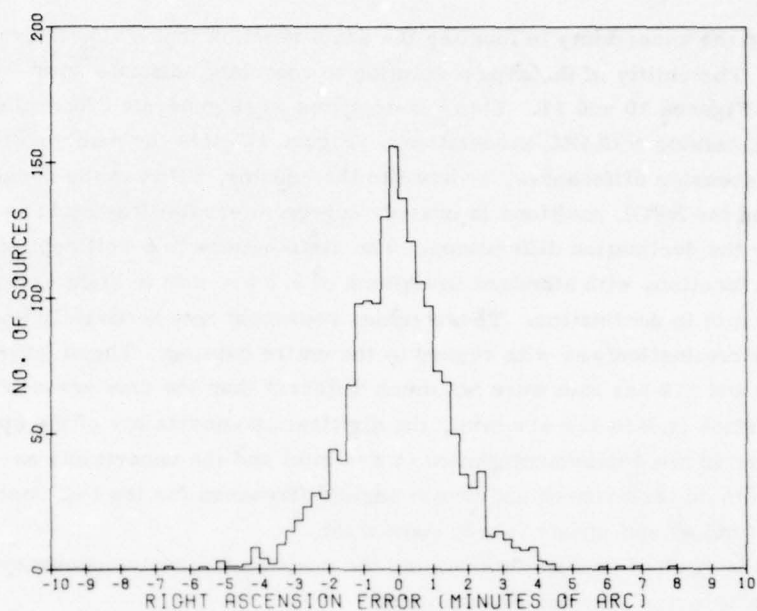
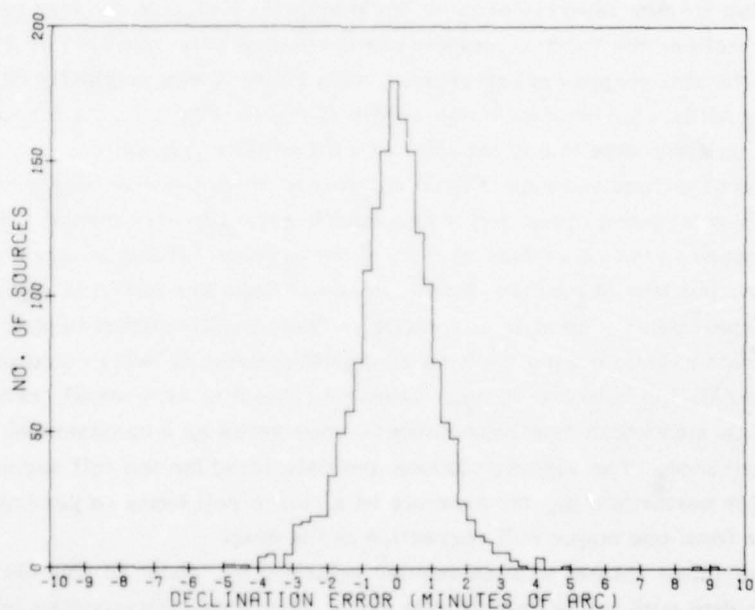


Figure 9. The Distributions in the Calculated Uncertainties in Declination for the Sources in the AFGL Catalog





**Figure 10.** The Distribution of the Differences Between Right Ascensions, Reduced to the Equator, of IRC<sup>6,7</sup> Sources in the AFGL Catalog and the Listed Position Either in the IRC<sup>6,7</sup> or the SAO<sup>8</sup> Catalog



**Figure 11.** A Histogram of the Differences in the Declination of AFGL Sources and the IRC<sup>6,7</sup> Objects Associated With Them

incorporated the uncertainty in locating the exact position that a source transited a detector. The ability of the aspect solution to calculate adequate source positions is shown in Figures 10 and 11. These histograms were generated from the sources in the AFGL catalog with IRC associations. Figure 10 plots the number of stars with right ascension differences, reduced to the equator, between the updated IRC positions and the AFGL positions in quarter degree intervals; Figure 11 is a similar plot for the declination differences. The distributions are well represented by gaussian functions with standard deviations of 1.5 arc min in right ascension and 1.2 arc min in declination. These values represent how accurately the method of aspect determination was with regard to the entire catalog. The standard deviations of 1.5 and 1.2 arc min were not much different than the rms error of the azimuth solution (1.0 to 1.5 arc min), the digitization uncertainty of the optical shaft encoder on the deployment gimbal (1 arc min) and the uncertainty associated with the limits on the azimuth and zenith angle differences for the IRC associations used in the final aspect update (about 1 arc min).

Thus, the desired goal of determining the position to greater accuracy than the size of a detector element was achieved.

## 7. COMPLETE ATTITUDE DETERMINED WITH THE STAR MAPPER

If the star tracker failed to acquire, or maintain, lock onto the star used for the pole of rotation, the inertial location of the rotation axis may also be determined from the star mapper observations. This solution was originally developed for the early AFGL experiments which used roll stabilized platforms for inertial guidance but is applicable to any experiment with similar geometry.

To extract the required aspect from the observations the star mapper must be accurately referenced to the defined geometric axis with star mapper "N" slit carefully mapped in the coordinate system of the payload. It is also assumed that the geocentric position of latitude, longitude and altitude are known at anytime during the experiment. The pole of rotation is taken to be constant in the body fixed coordinate system during the time an aspect solution is being calculated. Further, the rotation is either unconstrained or subject to very small, randomly timed perturbations which may reasonably be considered as a constant and continuous disturbance. The aspect solutions are calculated for the roll segments between major perturbations, for example on a roll to roll basis as previously described or from one major roll correction to the next.

The experiment rotates with an angular velocity,  $\omega_e$ , about an axis close to, but not coincident with the geometric roll axis. This geometry is shown in Figure 12 where  $\bar{R}_3$  is the geometric roll axis of the payload and  $\bar{R}_1$  is defined by the

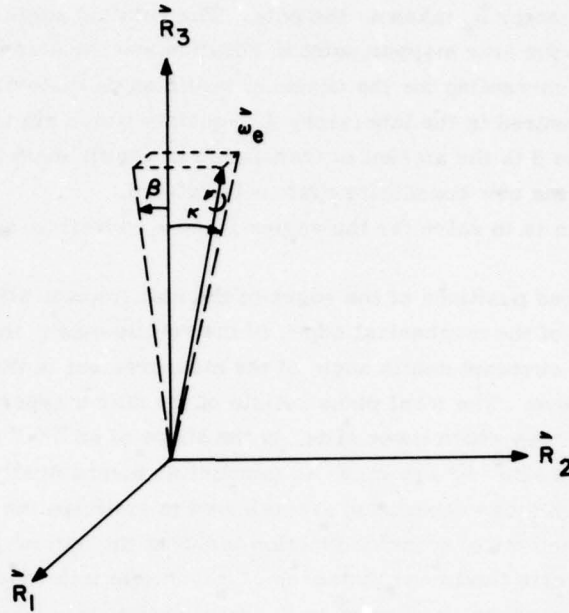


Figure 12. The Geometry of the Experiment. The defined payload longitudinal axis is in the direction of the vector  $\vec{R}_3$  and the star mapper reference is along  $\vec{R}_1$ . The experiment rotates about the true roll axis,  $\vec{\omega}_e$ , which is resolved into a tip off angle,  $\beta$ , in the  $\vec{R}_3 - \vec{R}_1$  plane and a rotation angle,  $\kappa$

star mapper azimuth reference point. The sensor deployment is in the  $\vec{R}_1 - \vec{R}_3$  plane. The rotation axis,  $\vec{\omega}_e$ , is resolved into a tipoff angle,  $\beta$ , in the  $\vec{R}_1 - \vec{R}_3$  plane and a skew angle  $\kappa$ , in the  $\vec{R}_2 - \vec{R}_3$  plane. Both  $\beta$  and  $\kappa$  are constrained to be small enough that the first order trigonometric approximations apply to them. Also, in order to obtain a tractable approach to the aspect solution, the measured positions of the reticle slit edges, corrected for cosecant zenith angle distortion, are assumed to be rectilinear in coordinate transformation. This means that the zenith and rotation angles of the slit edges in the coordinate system with  $\vec{\omega}_e$  as the pole may be found from

$$A_\omega = A_o \cos \kappa + (z_o + \beta) \sin \kappa = A_o + (z + \beta)\kappa \quad (9a)$$

$$z_\omega = -A_o \sin \kappa + (z_o + \beta) \cos \kappa = -A_o \kappa + (z + \beta) \quad (9b)$$

$A_o$  and  $z_o$  are the rotation and zenith angles of the star mapper point in question measured in the geometric reference frame and  $A_\omega$  and  $z_\omega$  are the corresponding

values with the vector  $\vec{\omega}_e$  taken as the pole. The rotation angle is the azimuth difference between the star mapper point in question and the star mapper azimuth reference after correcting for the cosecant zenith angle distortions. Thus, if  $\gamma$  is the angle measured in the laboratory  $A_0$  equals  $\gamma$  times  $\sin z$ . In the small angle assumption  $\beta$  is the amount of translation in zenith angle from the origin and  $\kappa$  is the amount the new coordinate system is rotated.

The problem is to solve for the angles  $\beta$  and  $\kappa$  as well as azimuth as a function of time.

The measured positions of the edges of the star mapper slits are the result of a convolution of the mechanical edges of the reticle mask, the optical transfer function and the cosecant zenith angle of the measurement in the defined geometric frame of reference. The focal plane reticle of the star mapper is a blackened copper plate through which three slits, in the shape of an "N," have been etched. The outer legs of this "N" are made as parallel as mechanically possible. The slit widths, heights and separation are selected to optimize the resolution for each experiment. The optical transfer function includes the optical gain and lens distortion and converts the linear distances of the reticle into angular distances. The angle between two slits, designated by  $\Omega$ , is related to the angle measured at a given zenith angle by

$$\gamma = \Omega / \sin z \quad (10)$$

The zenith angle of a star transiting the star mapper field is uniquely determined by the ratio of the angle between the first and second pulses and the first and third. For the situation where the geometric and dynamic rotation axis coincide this ratio is

$$\Omega_{12}/\Omega_{13} = \frac{\Omega_{12}/\sin z}{\Omega_{13}/\sin z} = \gamma_{12}/\gamma_{13} \quad (11)$$

which is independent of the cosecant distortion. Therefore, the measured angles  $\gamma_{12}$  and  $\gamma_{13}$  may be used directly in the zenith angle determination. Indeed this is precisely how the zenith angle function is obtained. The laboratory measurements described in the section on star mapper calibration are used to determine the functional relations which are needed to calculate the azimuth and zenith angle of the observed star.

First, the rotation angle as a function of zenith angle is calculated for each slit edge by means of a least square regression on the measured data. The curve fits for the two slit edges are averaged to obtain an expression for the rotation



angle of the center of each slit in terms of zenith angle. The peak of the pulse due to a star transiting a slit is assumed to occur at the slit center. The azimuth of an observed star pulse is equal to the azimuth of the star mapper reference point plus the rotation angle for the slit the star transits. The rotation angle is obtained from the known zenith angle of the transit and the rotation angle calibration.

The zenith angle is also calibrated through a least square regression on the zenith angle as a third order function of the ratio of the measured rotation angles of the first and second slits to the first and third. This is the ratio  $\gamma_{12}/\gamma_{13}$  in Eq. (11). The advantage of an N slit reticle over a "V" slit reticle is evident. Both give zenith angle information but the N slit measurements are independent of the cosecant distortion. The star mapper may, therefore, be translated in the  $\vec{R}_1 - \vec{R}_3$  plane such as when the rotation pole,  $\vec{\omega}_e$ , has a  $\beta$  component only, that is,  $\kappa$  equal zero, and the zenith angle calibration can be used to calculate the correct zenith angle of transit with respect to the geometric axis. As will be developed the angle of translation,  $\beta$ , is determined from the observed zenith angles for a number of stars.

The general case is shown in Figure 13 where a star at a constant zenith angle from the rotation pole  $\vec{\omega}_e$  tracks across the N slit elevated, or depressed, by an angle  $\beta$  and tilted by  $\kappa$ . In the absence of lens distortions, which were very small for the AFGL star mapper, the distance between slits a and b along the track of the star is

$$\Omega_{ab}/\cos \kappa .$$

The observed angular difference includes the cosecant distortion with respect to the pole of rotation

$$\gamma'_{ab} = \Omega_{ab}/\cos \kappa \sin z_{\omega} \quad (12)$$

where  $z_{\omega}$  is given by Eq. (9b). Eq. (12) becomes

$$\gamma'_{ab} = \Omega_{ab}/\cos \kappa \sin (z_o + \beta - A_o \kappa)$$

and  $A_o$  is the rotation angle of the central slit. Here again, the ratio of the first and second to the first and third slit angular differences cancels out the common denominator in Eq. (13) and we have

$$\gamma'_{21}/\gamma'_{31} = \Omega_{21}/\Omega_{31} .$$

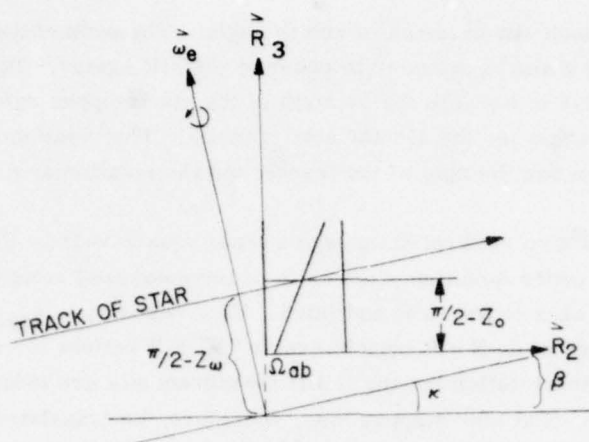


Figure 13. Geometry of a Star Transit. With respect to the true pole of rotation, the star mapper reticle is elevated by an amount  $\beta$  and rotated through an angle  $\kappa$ . The track of the star across the reticle is tilted at an angle  $\kappa$  with the result that the apparent rotation rate is slower than actually shown

Thus, the height of a stellar transit in the geometric reference frame is uniquely determined by the angular differences of the observed slit transits and does not depend on the knowledge of the orientation of true pole of rotation. This is only correct if  $\beta$  and  $\kappa$  are small enough that the small angle trigonometric approximations are applicable and the width of the N reticle is narrow enough that the small angle approximation applies to the measured rotation angles in the coordinate transformation.

Some "a priori" knowledge about the roll rate is required to convert the times of the observed pulses into angles. The angle between two slits is calculated from

$$\gamma_{21} = \omega_e(t_2 - t_1)/\sin z .$$

Once more, the ratio of  $\gamma_{21}/\gamma_{31}$  used to calculate the geometric zenith angle eliminates a constant roll rate. Expressly

$$\frac{\gamma_{12}}{\gamma_{13}} = \frac{\omega_e(t_2 - t_1)}{\omega_e(t_3 - t_1)} = \frac{t_2 - t_1}{t_3 - t_1} \quad (14)$$

and the ratio is obtained directly from the observed time difference.

Thus, for the "N" slit the exact value of a constant roll rate need not be known, only that it is constant. This is another advantage over the "V" slit for which the

exact roll rate has to be known in order to obtain the correct zenith angle. Further, if roll acceleration are small and the legs of the N are close together, the roll rate is essentially constant during a star transit across the reticle. In this case, the roll acceleration will appear in the aspect solution as producing a different "constant" roll rate for stars observed at different times. Also, since the time rate of change is the important variable in the ratio calculation, that is,

$$\frac{\gamma_{12}}{\gamma_{13}} = \frac{\left[ \omega_e(t_2 - t_1) + 1/2 \omega'_e(t_2^2 - t_1^2) \right] / \sin z}{\left[ \omega_e(t_3 - t_1) + 1/2 \omega'_e(t_3^2 - t_1^2) \right] / \sin z} = \frac{(t_2 - t_1)}{(t_3 - t_1)} \frac{1 + \frac{\omega'_e}{\omega_e} \frac{t_2 + t_1}{2}}{1 + \frac{\omega'_e}{\omega_e} \frac{t_3 + t_1}{2}}$$

an accurate value of  $\omega'_e/\omega_e$  might be obtained from the attitude control roll rate gyroscope readouts as the ACS calibration constants are cancelled in this ratio.

Thus, one set of observed inputs is obtained, the observed zenith angles in the rocket geometric reference frame from the times of the slit transits for the measured stars. The second set of input information remains to be considered, the positions of the observed stars in the expected reference frame of the experiment. The two most commonly used coordinate systems for rocket and balloon experiments are the inertial and geometric.

Inertial guidance produced by roll stabilized platforms, is designed to maintain a constant reference with respect to the "fixed" stars. This is the situation for the AFGL experiments where the rotation axis is constrained by the star tracker to the celestial, that is, inertial, coordinates of the "pole" star. The launch time and the attitude control system are programmed to obtain the inertial position of the star before control is transferred to the tracker. If the tracker fails to acquire, or loses lock, the attitude control system maintains the programmed reference. For some experiments an "a priori" establishment of the inertial coordinates may not be critical or necessary. In this case, the inertial reference may be found from the programmed relative position of the attitude control system and the sidereal time when the attitude gyroscopes are uncaged.

For long duration experiments, such as balloon flights, or earth centered experiments to measure the earth's limb, a geocentric coordinate system is applicable. The inertial pole of the payload is constantly changing and the latitude and longitude need to be accurately known as a function of time as well as the relative geometry of the experiment in order to calculate the inertial coordinates applicable.

For convenience, the celestial coordinates of right ascension ( $\alpha$ ) and declination ( $\delta$ ) may be used to designate the position in inertial coordinates. Let  $\alpha_p$  and  $\delta_p$  be the right ascension and declination, respectively, of the inertial pole defined for the experiment in celestial coordinates. Then  $\alpha_*$  and  $\delta_*$  are the right ascension and declination, respectively, of the observed star. For the case of the "a priori" determined inertial reference,  $\alpha_p$  and  $\delta_p$  are defined for the experiment. For an inertial platform which is launched at a sidereal time  $\theta_0$  and an inertial reference  $\lambda$  longitude and  $\phi$  latitude,

$$\alpha_p = \theta_0 - \lambda \quad (15a)$$

$$\delta_p = \phi \quad (15b)$$

The above expressions are also applicable to the geocentric situation except that each of the variables are functions of time and the pole has to be calculated for each stellar observation.

The standard spherical trigonometric formulae apply to determine the azimuth and zenith angle of the observed star with respect to the pole at  $(\alpha_p, \delta_p)$

$$\cos z_* = \sin \delta_* \sin \delta_p + \cos \delta_* \cos \delta_p \cos (\alpha_* - \alpha_p) \quad (16)$$

$$\cos Az_* = \frac{\sin \delta_* - \sin \delta_p \cos z_*}{\sin z_* \cos \delta_p} \quad (17)$$

$$\sin Az_* = -\cos \delta_* \sin (\alpha_* - \alpha_p) / \sin z_* \quad (18)$$

Since the location of the anticipated pole of rotation  $(\alpha_p, \delta_p)$  is known and Eqs. (16), (17) and (18) gives the azimuth and zenith angle of the brighter stars, a sequence of star mapper observations may be generated and at least the brighter pulses may be associated with the stars which cause them. The actual pole of rotation is tipped off the anticipated inertial pole by an amount,  $\epsilon$ , in a direction which is at an angle,  $\eta$ , away from the north point as shown in Figure 14. The observed ratio of the times between the first and second to first and third pulses from a star permits a calculation of the geometric zenith angle for that star. This, in turn is related to the zenith angle with respect to the pole of rotation through the unknowns,  $\beta$  and  $\kappa$ , as defined in Eq. (9b).



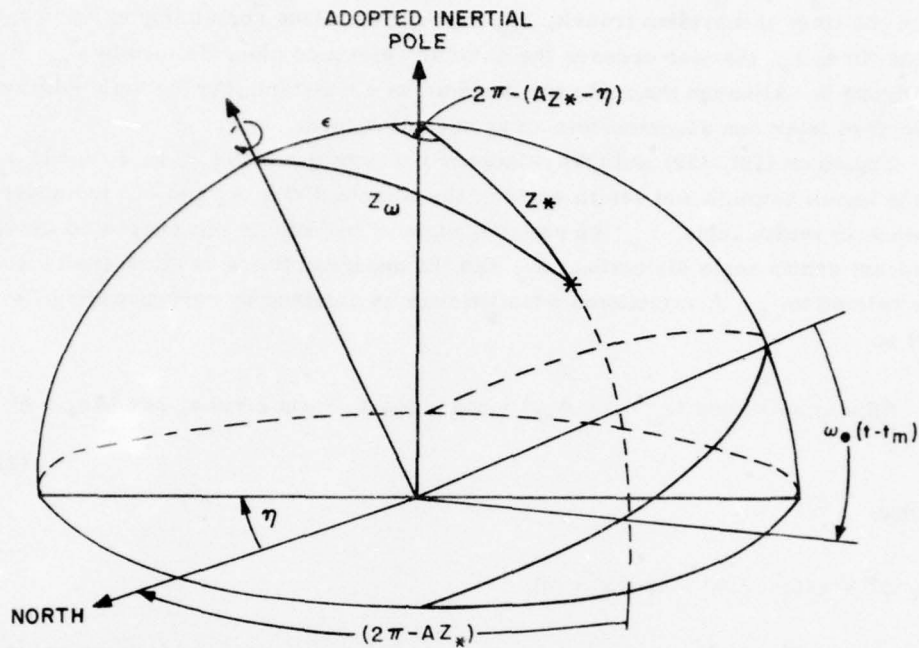


Figure 14. Pole of Rotation in Inertial Coordinates. The pole of rotation,  $\vec{\omega}_e$ , is offset by an angle  $\epsilon$  from the adopted inertial pole in the direction which is rotated by an angle,  $\eta$ , from the north point. The zenith angle and azimuth,  $z_*$  and  $Az_*$  respectively, of the observed star are calculated quantities from the known inertial coordinates of the star and the adopted pole. The star transits the star mapper at a zenith angle,  $z_\omega$ , after the star mapper reference has swept through an angle  $\omega_e(t - t_m)$  from meridian transit

The spherical trigonometric relationships for the situation shown in Figure 14 are

$$\begin{aligned} \cos z_* &= \cos z_\omega \cos \epsilon + \sin z_\omega \sin \epsilon \cos \omega_e(t_* - t_m) \\ &= \cos(z_o + \beta - A_{o\kappa}) \cos \epsilon + \sin(z_o + \beta - A_{o\kappa}) \sin \epsilon \cos \omega_e(t_* - t_m) \end{aligned} \quad (19)$$

$$\cos z = \cos(z_o + \beta - A_{o\kappa}) = \cos \epsilon \cos z_* + \sin \epsilon \sin z_* \cos(Az_* - \eta) \quad (20)$$

$$\begin{aligned} \sin \omega_e(t_* - t_m) / \sin z_* &= -\sin(Az_* - \eta) / \sin z_\omega \\ &= -\sin(Az_* - \eta) / \sin(z_o + \beta - A_{o\kappa}) . \end{aligned} \quad (21)$$

Here  $\omega_e (t_* - t_m)$  is the angle swept out by the rotation, at a roll rate  $\omega_e$ , from the time of meridian transit,  $t_m$ , through the plane containing both poles, to the time,  $t_*$ , the star crosses the azimuth reference plane defined by  $\vec{\omega}_e - \vec{R}_1$  in Figure 9. Although the roll rate is shown as a constant, the azimuth solution described later can accommodate an acceleration term.

Equations (19), (20) and (21) relate the unknown quantities  $\beta$ ,  $\kappa$ ,  $\epsilon$ ,  $\eta$  and  $\omega_e$  to the known azimuth and zenith angle of the observed star  $A_*$  and  $z_*$ , the observed geometric zenith angle,  $z_o$ , the rotation angle of the middle slit corrected for the cosecant zenith angle distortion,  $A_o$ , and the observed times of slit transits which are related to  $t_*$ . A variational equation may be obtained by re-expressing Eq. (20) as

$$f(\beta, \kappa, \epsilon, \eta) = -\cos(z_o + \beta - A_o \kappa) + \cos \epsilon \cos z_* + \sin \epsilon \sin z_* \cos(Az_* - \eta) \quad (22)$$

Define

$$\Delta f \equiv f_i(\beta, \kappa, \epsilon, \eta) - f_T(\beta, \kappa, \epsilon, \eta)$$

where  $f_T$  is Eq. (22) with the correct values of the unknowns and  $f_i$  is the value of  $f$  with the  $i^{\text{th}}$  guess of the variables. Note that by definition from Eq. (20)  $f_T$  equals zero. Also

$$\Delta f = \frac{\partial f}{\partial \beta} \Delta \beta + \frac{\partial f}{\partial \kappa} \Delta \kappa + \frac{\partial f}{\partial \epsilon} \Delta \epsilon + \frac{\partial f}{\partial \eta} \Delta \eta$$

where

$$\frac{\partial f}{\partial \beta} = +\sin(z_o + \beta - A_o \kappa)$$

$$\frac{\partial f}{\partial \kappa} = -A_o \sin(z_o + \beta - A_o \kappa)$$

$$\frac{\partial f}{\partial \epsilon} = -\sin \epsilon \cos z_* + \cos \epsilon \sin z_* \cos(Az_* - \eta)$$

$$\frac{\partial f}{\partial \eta} = +\sin \epsilon \sin z_* \sin(Az_* - \eta)$$

then

$$\begin{aligned} \Delta f = & \sin(z_0 + \beta - A_0 \kappa)(\Delta\beta - A_0 \Delta\kappa) + (\cos \epsilon \sin z_* \cos(Az_* - \eta) \\ & - \sin \epsilon \cos z_*)\Delta\epsilon + \sin \epsilon \sin z_* \sin(Az_* - \eta)\Delta\eta . \end{aligned} \quad (23a)$$

The  $\kappa$  term is coupled with the geometric rotation angle,  $A_0$ , of the center slit of the transit. The term  $A_0$  varies from about 0.01 to 0.1 radians (see Figure 3) which implies that in the general situation where  $\beta$  and  $\kappa$  are roughly comparable,  $A_0 \kappa$  is significantly less than  $\beta$  and the variation  $A_0 \Delta\kappa$  is not important in Eq. (23a). It is also necessary to eliminate one of the correction terms since the cross coupling cause problems with the solution converging. Eq. (23a) therefore may be written

$$\begin{aligned} f = & \sin(z_0 + \beta - A_0 \kappa)\Delta\beta + (\cos \epsilon \sin z_* \cos(Az_* - \eta) - \sin \epsilon \cos z_*)\Delta\epsilon \\ & + \sin \epsilon \sin z_* \sin(Az_* - \eta)\Delta\eta \end{aligned} \quad (23b)$$

where  $\kappa$  is taken as a constant and initially assumed to be zero.

A good initial estimate of the variables  $\beta$ ,  $\epsilon$  and  $\eta$  is obtained as follows: Assume  $z \approx \pi/2$  and define the quantity,  $\Delta z$  as

$$\Delta z \equiv z_* - z_0$$

Now if  $\Delta z$  is small,  $\epsilon$  and  $\beta$  will be small and the small angle trigonometric approximations applied to Eq. (20) give

$$\Delta z = z_* - z_0 = \beta + \epsilon \cos(Az_* - \eta) . \quad (24)$$

A value for  $\Delta z$  and  $Az_*$  is obtained for each star transit and the initial values of  $\beta$ ,  $\epsilon$ , and  $\eta$  are calculated through a least squares fit of the observations to Eq. (24). The quantity  $f = f(\beta, \kappa, \epsilon, \eta) - f_T(\beta, \kappa, \epsilon, \eta)$  is calculated with these initial values and a linear regression is performed on Eq. (23b) to obtain the correction terms  $\Delta\beta$ ,  $\Delta\epsilon$  and  $\Delta\eta$ . Note again that  $f_T(\beta, \kappa, \epsilon, \eta)$  is the exact solution and equals zero by definition. The unknown variables are incremented to obtain updated values

$$\beta_{i+1} = \beta_i + \Delta\beta_i$$

$$\epsilon_{i+1} = \epsilon_i + \Delta\epsilon_i \quad \text{values in radians}$$

$$\eta_{i+1} = \eta_i + \Delta\eta_i$$

The variational equation is updated, that is,

$$f_{i+1}(\beta, \epsilon, \kappa, \eta) = -\cos(z_o + \beta_{i+1} - A_o \kappa) + \cos \epsilon_{i+1} \cos z_* + \sin \epsilon_{i+1} \sin z_* \cos(Az_* - \eta_{i+1})$$

and

$$\begin{aligned} f_{i+1}(\beta, \epsilon, \kappa, \eta) = & \sin(z_o + \beta_{i+1} - A_o \kappa) \Delta\beta + (\cos \epsilon_{i+1} \sin z_* \cos(Az_* - \eta_{i+1}) \\ & - \sin \epsilon_{i+1} \cos z_*) \Delta\epsilon - \sin \epsilon_{i+1} \sin z_* \sin(Az_* - \eta_{i+1}) \Delta\eta \end{aligned} \quad (25)$$

and a new least square regression is used to obtain a new set of correction terms which are used to update the variables which, in turn, leads to a new variation equation. The process is iterated until the new set of correction terms is sufficiently small.

The next step is to determine the roll rate,  $\omega_e$ , the meridian transit time  $t_m$  and the angle  $\kappa$ . Equation (21) may be rewritten:

$$\omega_e(t_* - t_m) + \frac{1}{2} \omega_e'(t_j^2 - t_m^2) = \arcsin \left\{ -\frac{\sin(Az_* - \eta) \sin z_*}{\sin(z_o + \beta - A_o \kappa)} \right\} \quad (26)$$

$$+ A_\omega / \sin(z_o + \beta - A_o \kappa) \quad (26)$$

$t_j$  is the time of the  $j^{\text{th}}$  star mapper pulse and is equal to the time of the star transit of the reference plane,  $t_*$ , plus the time to rotate to the middle slit.

Now, from Eq. (9a)

$$A_\omega = A_o + (z_o + \beta)\kappa$$

$A_o$  is the geometric rotation angle of the slit, corrected for the apparent cosecant distortion, and is determined through the mapper azimuth calibration and from the observed geometric zenith angle. In Eq. (26) the time of slit transit now depends on the observed height  $(z_o + \beta)$  through the angle  $\kappa$  which allows a direct determination of  $\kappa$ . Expressly Eq. (26) becomes



$$\omega_e(t_j - t_m) + \frac{1}{2} \omega_e'(t_j^2 - t_m^2) - [A_o + (z_o + \beta)\kappa] / \sin(z_o + \beta - A_o\kappa) =$$

$$\arcsin \left\{ \frac{-\sin(Az_* - \eta) \sin z_*}{\sin(z_o + \beta - A_o\kappa)} \right\} \quad (27)$$

which is solved through a least square regression, with observed and known variables and the values of  $\beta$ ,  $\epsilon$  and  $\eta$  obtained previously, to find  $\omega_e$ ,  $\omega_e'$ ,  $t_m$  and  $\kappa$ . Initially  $\kappa$  is assumed to be zero in the argument for the sine. The value of  $\kappa$  from Eq. (27) is used in Eq. (23b) to iterate to a new solution for a new set of  $\beta$ ,  $\epsilon$  and  $\eta$ . These values, in turn, are used in Eq. (27), along with the current value of  $\kappa$ , to derive a new set of  $\omega_e$ ,  $\omega_e'$ ,  $t_m$  and  $\kappa$ . This procedure continues until the changes in the derived variables fall below specified limits.

It may be that the spin vector,  $\vec{\omega}_e$ , is not fixed in the external reference frame. Such is the case for good inertial guidance platforms which drift about a tenth of a degree per minute. Thus, for slow scan speeds or long time intervals this change may become significant. This situation can be handled in the present development for the limited case where

$$\epsilon(t) = \epsilon + \epsilon't$$

$$\eta(t) = \eta + \eta't$$

with  $\epsilon'$  and  $\eta'$  constant.

The time,  $t$ , in these equations is measured with respect to a known reference time. Usually, this reference is either the time of launch or the time for the beginning of the data section for which an aspect solution is being derived. For convenience, it is assumed that the slit transit times are referred to this same initial time.

Equation (22) becomes

$$f = \cos(\epsilon + \epsilon't_*) \cos z_* + \sin(\epsilon + \epsilon't_*) \sin z_* \cos(Az_* - \eta - \eta't)$$

$$- \cos(z_o + \beta - A_o\kappa) \quad (28)$$

The approximation to obtain the initial values of the variables is

$$\Delta z = z_o - z_* = \beta + (\epsilon + \epsilon't_*) \cos(Az_* - \eta) + \epsilon\eta't \sin(Az - \eta)$$

The variational equation (Eq. 23b) is now

$$\begin{aligned} \Delta f = & [\cos z_* \sin (\epsilon + \epsilon' t_*) - \sin z_* \cos (\epsilon + \epsilon' t_*) \cos (Az_* - \eta - \eta' t_*)][\Delta \epsilon + t_* \Delta \epsilon'] \\ & - [\sin z_* \sin (\epsilon + \epsilon' t_*) \sin (Az_* - \epsilon - \epsilon' t_*)][\Delta \eta + t_* \Delta \eta'] \\ & - \sin (z_o + \beta - A_o \kappa) \Delta \beta \end{aligned} \quad (29)$$

which is solved by the iterative procedures described previously. Note, however, that  $t$  is the time of transit through the attitude reference in the  $\bar{R}_1 - \bar{\omega}_e$  plane. The observed time of the first slit crossing,  $t_j$ , is related to  $t_*$  through the rotation rate and the rotation angle  $A_\omega$ . The first iterated solution is done assuming  $t_j$  equal to  $t_*$ .

The equivalent to Eq. (27) is

$$\begin{aligned} \omega_e [t_j - t_m(t)] - \frac{1}{2} \omega_e' [t_j^2 - t_m^2(t)] - [A_o + (z_o + \beta)\kappa] / \sin (z_o + \beta - A_o \kappa) \\ = \arcsin \left\{ \frac{-\sin (Az_* - \eta - \eta' t_*) \sin z_*}{\sin (z_o + \beta - A_o \kappa)} \right\}. \end{aligned} \quad (30)$$

The time of meridian transit varies due to changes in the azimuthal angle,  $\eta$ , to the north point. This results in an apparent acceleration of roll rate due to the changing coordinate system. For small changes,  $t_m(t) \simeq t_m + (dt_m/dt)t$  and the change of meridian transit time is given by the small angle approximation

$$\omega_e t_m' = \cos (\epsilon + \epsilon' t) \eta'$$

Substituting this expression into Eq. (30) to eliminate the time dependence of  $t_m$  we have

$$\begin{aligned} \omega_e [t_j - t_m] + \frac{1}{2} \omega_e [t_j^2 - t_m^2] - \cos (\epsilon + \epsilon' t_j) \left( 1 + \frac{\omega_e'}{\omega_e} \right) \eta' t_j - \frac{A_o + (z_o + \beta)\kappa}{\sin (z_o + \beta - A_o \kappa)} \\ = \arcsin \frac{-\sin (Az_* - \eta - \eta' t_*) \sin z_*}{\sin (z_o + \beta - A_o \kappa)}. \end{aligned} \quad (31)$$

As before, a least square regression on Eq. (30) with the known variables  $Az_*$ ,  $z_*$ , the observed  $z_o$  and  $A_o$  and the derived values of  $\beta$ ,  $\epsilon$ ,  $\epsilon'$ ,  $\eta$  and  $\eta'$  will determine the  $\omega_e$ ,  $\omega_e'$ ,  $t_m$  and  $\kappa$ . The  $\kappa$  term is substituted as a constant in Eq. (29) and a new iterated least square solution is obtained for the unknown variables  $\beta$ ,  $\epsilon$ ,  $\epsilon'$ ,  $\eta$  and  $\eta'$ . If needed, the times used in Eq. (29) are corrected from time of slit transit to time of reference plane transit by

$$t_* = t_j - \frac{A_o + (z_o + \beta)\kappa}{\sin(z_o + \beta - A_o\kappa)} \bigg/ \omega_e \left( 1 + \frac{\omega_e'}{\omega_e} t_j \right) (1 - \cos(\epsilon + \epsilon' t_j) \eta) .$$

The new set of iterated variables are used in a new regression on Eq. (31) to update the values of  $\omega_e$ ,  $\omega_e'$ ,  $t_m$  and  $\kappa$ . These iterations continue until the derived correction values are sufficiently small.

The equations used to obtain the aspect, Eq. (23b) and (26) for the fixed reference system and Eq. (29) and (31) for the time dependent case, are decidedly non-linear and therefore the requirement for an iterated solution. As with any non-linear equation care must be taken that the initial values are accurate enough and the correction terms are sufficiently uncoupled such that the interactions drive the solution to the global minimum rather than a local one. The  $\Delta\kappa$  term was eliminated in Eq. (23b) to prevent the coupling with the  $\Delta\beta$  term. Also, reducing the order in the multiple variable regressions with "a priori" knowledge will reduce the number of "local" minima. For instance, the relative variation in roll rate possibly may be obtained independently of the calibration of the attitude control system telemetry. If this ratio were known, Eq. (26) and (31) could be rewritten to express this ratio in terms of the unknown roll rate, thus reducing the multiple variable order of these equations by one.

## 8. RESULTS AND CONCLUSIONS

The AFGL infrared sky survey experiments were able to obtain an arc min knowledge of the line of sight of the survey telescope with respect to the payload defined coordinate system through careful payload design and meticulous alignment procedures to calibrate the outputs of the aspect sensors. A fine error guidance sensor aligned to the defined payload roll axis held an inertial reference to within 20 arc sec during the experiment and, therefore, maintained the alignment accuracy under transformation to inertial coordinates.

An azimuth solution, in inertial space, was obtained expressing angle of the defined azimuth reference plane as a function of time from a least square regression of stellar transits observed by a star mapper with an "N" slit reticle mask.



These solutions typically had root mean square deviations between the calculated and observed position of 1.5 to 2.5 arc min. This compares favorable with the slit width of 9 arc min.

The data from the infrared sensor on sources associated with previously cataloged objects were used to obtain the inflight offsets from the laboratory calibration of deployment angle and azimuth on a roll to roll basis for each flight. In most cases a simple average of the azimuth and zenith angle differences were used to calculate the offsets for the center of the telescope from those predicted from the laboratory calibration and the star mapper azimuth aspect. In almost all cases the final root mean square of the difference between the observed and predicted azimuth was one to one and a half arc min. This translates into an rms uncertainty of about 1.4 data samples which was empirically found to be the size of the position error box necessary to successfully combine multiple observations. It is also roughly equal to the time of half width at half height of a typical point source signal. The zenith angle rms value of three arc min is exactly equal to the uncertainty in determining the transit zenith angle for a 10.5 arc min high detector.

The ultimate accuracy to the positions assigned to the infrared detections were set by the size of a detector resolution element and not by the experimental geometry. Thus, one of the important design goals for the payload was achieved.

Each of the aspect sensors were backed up by alternate, lower accuracy, aspect devices. Generally, the attitude control systems pitch, roll and yaw position and rate gyroscopes could be used. However, a method of complete aspect determination for the payload from the star mapper was developed in detail owing to the wide range of experiments to which it is applicable. A preliminary version of this development was used to obtain the payload aspect for the early proof of concept experiments flown at AFGL. The aspect solution for these flights were able to reproduce the observed star mapper sightings to within a fraction of a degree. Some refinement is anticipated for the current development since the skew angle  $\kappa$  and roll acceleration  $\omega_e'$  were not included in previous solutions.



## References

1. Walker, R.G., and Price, S.D. (1975) AFCRL Infrared Sky Survey: Volume I. Catalog of Observations at 4, 11 and 20 Microns, AFCRL-TR-75-0373.
2. Price, S.D., and Walker, R.G. (1976) The AFGL Four Color Infrared Sky Survey: Catalog of Observations at 4.2, 11.0, 19.8 and 27.4  $\mu\text{m}$ , AFGL-TR-76-0208.
3. Price, S.D. (1977) The AFGL Four Color Infrared Sky Survey: Supplemental Catalog, AFGL-TR-77-0160.
4. Price, S.D., Cuniff, C.V., and Walker, R.G. (1978) Cleanliness Considerations for the AFGL Infrared Celestial Survey Experiments, AFGL-TR-78-0171.
5. Hoffleit, D. (1964) Catalog of Bright Stars, 3rd Edition, Yale University Observatory.
6. Neugebauer, G., and Leighton, R.B. (1969) Two Micron Sky Survey, A Preliminary Catalog, NASA SP-3047.
7. Neugebauer, G. (1971) Extension to the Two Micron Sky Survey, unpublished.
8. Smithsonian Astrophysical Observatory (1966) Star Catalog, Smithsonian Publication 4652, U.S. Government Printing Office.

## Appendix

### Definition of Terms

- $\vec{R}_3$  - The vector along the geometric longitudinal, or roll, axis of the experiment.
- $\vec{R}_1$  - The vector, orthogonal to  $\vec{R}_3$ , in the direction of the star mapper azimuth reference point.
- $\vec{\omega}_e$  - The vector along the actual spin axis of the experiment.
- $z_o$  - The geometric zenith angle measured from the vector  $\vec{R}_3$ .
- $A_o$  - The rotation angle between a point in the star mapper plane and the star mapper azimuth reference point. This angle is equal to the angle measured to that point in the laboratory times the sine of the measured geometric zenith angle.
- $z_\omega$  - The zenith angle with respect to the vector  $\vec{\omega}_e$ .
- $A_\omega$  - The rotation angle with  $\vec{\omega}_e$  as the pole.
- $\beta$  - The component of the vector  $\vec{\omega}_e$  in the  $\vec{R}_3 - \vec{R}_1$  plane. This is the tip off angle of the pole of rotation in the nominal deployment plane of the sensor.
- $\kappa$  - The component of  $\vec{\omega}_e$  in the  $\vec{R}_3 - \vec{R}_2$  plane. This is the skew angle of the star mapper when the experiment rotates about  $\vec{\omega}_e$ .
- $\Omega(z)$  - The rotation angle in geometric coordinates between two star mapper slits at a geometric zenith angle,  $z$ , after correcting for cosecant zenith angle distortion.

$\gamma(z)$	- The laboratory measured geometric rotation angle between two star mapper slits. This angle includes the cosecant distortion, that is, $\gamma = \Omega / \sin z$ .
$\epsilon$	- The angle between the rotation vector $\vec{\omega}_e$ and the pole in the defined inertial system.
$\eta$	- The angle between the plane through the inertial pole and the north point and the plane containing the inertial pole and the vector $\vec{\omega}_e$ .
$\omega_e$ and $\omega_e^t$	- The angular rotation and acceleration of the experiment about the pole of rotation, $\vec{\omega}_e$ .
$t_m$	- The time at which the azimuth reference point crosses the meridian.
$t_*$	- The time at which a star is in the azimuth reference plane.
$t_j$	- The time of the $j^{\text{th}}$ star pulse from the star mapper.
$\alpha$	- The celestial right ascension.
$\delta$	- The celestial declination.
$\phi$	- The geocentric latitude.
$\lambda$	- The geocentric longitude.
$\theta$	- The sidereal time.

